Near-infrared absorption spectrum of the Ar–HD complex: A theoretical study of predissociation effects

Felicja Mrugała[a)]
Institute of Physics, N. Copernicus University, Grudziądzka 5, 87-100 Toruń, Poland

(Received 14 September 2000; accepted 27 April 2001)

Results of close-coupling calculations on the near-infrared absorption by the Ar–HD($v=0,j=1$) complex, exploiting the best available empirical and theoretical models of intermolecular potential and of induced-dipole moment for Ar–H_2, are reported. The first quantitative description of the $S_1(1)$ band of the spectrum is given, including transition energies, linewidths, and intensities, and the description of the $Q_1(1)$ band, included in the recent study on Ar–HD [J. Chem. Phys. **109**, 10823 (1998)], is completed with calculation of the spectrum shape. A pattern of pairs of lines of distinct widths and heights is found in the *T*- and *N*-transition regions of the $S_1(1)$ band. The narrow lines in the pairs (widths $\sim 0.1-0.2\,\mathrm{cm}^{-1}$) result from transitions between bound and predissociating states. The wider lines (about 6–10 times) appear due to transitions between predissociating states. The relations between heights of lines in the pairs differ qualitatively from the relative intensities of the corresponding lines in the $S_1(1)$ band of the absorption spectrum of Ar–H_2. In the $Q_1(1)$ band, transitions between states predissociating rotationally are found to be the only ones which have discernible impact on the line contour. Results of this work and the recent results on the Ar–HD($v=0,j=0$) complex are summarized in a discussion of effects of the asymmetric isotopic substitution on the absorption spectrum shape. © *2001 American Institute of Physics.* [DOI: 10.1063/1.1379754]

I. INTRODUCTION

Ar–HD belongs to the earliest discovered[1] and the most thoroughly investigated family of van der Waals molecules.[2–9] As typical for this kind of molecules, the rovibrational energy spectrum of Ar–HD consists of relatively few truly bound state levels (20, as established recently[9]) and of numerous metastable states which can decay by tunneling (the quasibound states), by coupling between intra- and intermolecular vibrational and rotational modes of motion (the predissociating states), or by a combination of these mechanisms. Among the best-known complexes formed by hydrogen molecule isotopomers with noble gas atoms, the Ar–HD complex is distinguished by rapid decay through rotational predissociation (about two orders of magnitude faster than the rates characteristic for Ar–H_2 and Ar–D_2). From that stems the role of the Ar–HD complex as a benchmark weakly bound system for studying predissociation phenomenon.

There have been several stages in theoretical studies of the Ar–HD complex. The modeling of the electronic energy potential surface for the Ar+H_2 system was certainly the leading motive of the studies at their initial stage. At the time when the first measured predissociation widths in the near-infrared absorption spectrum of Ar–HD became available,[2] theoretical investigations of weak-anisotropy van der Waals molecules[10] revealed ''that predissociation level widths do ... contain information about the potential anisotropy which cannot be obtained from the level energies alone.'' Naturally, the first theoretical studies on predissociation in the Ar–HD complex were focused on calculation of the widths.[5,6] Making such calculations so efficient that the measured widths could be included in the iterative determination of empirical potentials was, and still is (cf. Ref. 11), a desirable goal to achieve. At the next stage, the scope of studies of the Ar–HD complex became considerably broadened by adoption of the view of the predissociation as resonances in the photodissociation process. Accurate photodissociation calculations have become possible due to the exploitation of the idea of artificial scattering channel[12] for numerical implementation of the rigorous theory of photodissociation of triatomic molecules, developed by Balint-Kurti and Shapiro.[13,14] Application of this theory to the Ar–HD complex resulted in the first simulation[7,8] of the predissociation limited shape of the $S_1(0)$ band in its absorption spectrum.

In the last decade, there have been remarkable developments in the determination of intermolecular potential surfaces of van der Waals complexes. Due to the development of the symmetry-adapted perturbation theory (SAPT) of intermolecular interactions (cf. Ref. 15 for a review), the first fully *ab initio* potential for the Ar–H_2 complex appeared in 1993.[16] In 1996 a new empirical potential for Ar–H_2, fitted to the most recent high-resolution discrete infrared spectra for Ar–H_2 and Ar–D_2,[3] was published;[17] it represents the first application of the sophisticated exchange-coulomb (XC) model to a three-dimensional atom-diatom potential surface. This new electronic structure information has naturally invoked a desire for assessing its quality by comparing to a possibly wide range of experimental data, and in particular, with the data for the predissociation widths in the Ar–HD complex. That was the goal of our recent study on the near-

a)Electronic mail: felicja@phys.uni.torun.pl

infrared absorption spectrum of the Ar–HD complex.[9] That study was also concerned with some purely dynamic aspects of the photoabsorption process (the role of transition from quasibound states), as this appeared necessary for achieving good consistency with the experiment on the theoretical shape of the $S_1(0)$ band of the spectrum.

The comparison of theory with experiment in Ref. 9 shows that theory can reliably investigate aspects of photoabsorption dynamics of the Ar–HD complex which are difficult to study experimentally with high accuracy. Of particular interest is absorption by this complex when HD is rotationally excited.[1,3] The corresponding parts of the spectrum in the near-infrared range are the bands accompanying the $Q_1(1)$ and $S_1(1)$ transitions in HD. These bands seem worthy of a deeper analysis for the following reasons:

(i) They involve predissociation effects which are more diverse than those occurring in the $S_1(0)$ band studied previously. The diversity results from the fact that both the final and the initial states of many transitions composing these bands can decay by rotational predissociation. Since the decay rates of initial and terminal states of the transitions vary over a wide range (cf. Ref. 9 and Sec. IV), the very nature of a van der Waals complex—as an intermediate between a typical (bound) molecule and a typical (free) collision system—is reflected. How this character manifests itself in the absorption spectrum shape is therefore a question of quite general importance. A recent simulation of the shape of the $S_1(0)$ band[9] revealing that some inconsistencies with experiment encountered in an earlier study[7,8] have origins quite different than was suspected shows that the answer to the question is not as obvious as it might seem.

(ii) Because of the abundance of transitions between rapidly predissociating states, an adequate simulation of the shapes of the $Q_1(1)$ and $S_1(1)$ bands becomes, to a large extent, a matter of the determination of resonance structures in the cross section for collision-induced absorption (CIA). Since the anisotropy of the intermolecular interaction is the cause of these structures, the rigorous version of the CIA theory for molecular gases[18,19] has to be applied. Applications of this version have been rare (see Ref. 20 for a review) because of computational expense, so improved ways of numerical implementation of the theory should be sought. This is, therefore, a good occasion to promote the idea of transplanting to the field of molecular CIA calculations the invariant imbedding techniques which, due to their stability and efficiency, are widely used in solving the coupled equations of the quantum theory of molecular collisions (see Ref. 21 and references therein). Though the idea itself seems obvious, it had not been tried till the recent calculations on the shape of the $S_1(0)$ band of Ar–HD[9] in which the log-derivative method,[22] generalized for the evaluation of first-order free–free transition amplitudes,[23] was exploited. Line-shape simulation of the $S_1(1)$ and $Q_1(1)$ bands is a considerably more demanding task, requiring evaluation of a greater number of phototransition amplitudes between multichannel free states which necessarily involve close-channel components. Thus, exploitation of the generalized log-derivative method in such a simulation can provide further evidence that the method is capable of facilitating the investigations of molecular collisions in a weak radiation field. Indeed, the method avoids direct evaluation of the initial and final state functions, and it does not require enlarging the system of the coupled equations which have to be simultaneously dealt with. Because of the latter feature it should be more efficient than the approach employed in the most recent calculations on the infrared absorption spectra by the H_2–He collision pairs, Ref. 24, being an adaptation of the close-coupling theory of atomic collisions in a radiation field of arbitrary strength.[25]

(iii) The overall shape of the $Q_1(1)$ band should be sensitive, much more than the shapes of the $S_1(0)$ and $S_1(1)$ bands, to the relative strengths of the two basic spherical components of the induced-dipole moment vector for Ar–H_2, the quadrupole-induced and the charge-induced terms.[26,27] Some new information may be expected to emerge from calculations of the shape of this band concerning adequacy of the empirical models of the induced dipole for Ar–H_2.[26,28]

The scope of investigations on the dynamics of photoabsorption by the Ar–HD complex is extended in this work to the $S_1(1)$ and $Q_1(1)$ bands so that the picture of predissociation effects exhibited by this benchmark system could be made more complete. The theory and the computational methodology used in the present investigations are basically the same as those applied in Ref. 9.

A. Contents of the paper

Since a sufficiently detailed description of the theory of photoabsorption dynamics by atom–diatom van der Waals complexes was presented in Ref. 9, only some necessary definitions are repeated in Sec. II of the present paper. More space is devoted to a description of the dynamic implications of the asymmetric isotopic substitution. Of particular interest is the influence of the enhanced rotational predissociation on the absorption spectrum shape. Attention is paid to effects which may appear because of the presence of transitions between predissociating states. In Sec. III, a description of calculations done in this work is given. It includes the most important details of the line-shape simulations of the predissociation limited spectrum of Ar–HD. In particular, information is given on the computational effort which was necessary for the inclusion of transitions between predissociating states. A part of the description is devoted to simulations of absorption spectrum contours limited by experimental resolution. Such simulations, for the Ar–H_2 complex, were also performed in the course of the investigations on the dynamics of Ar–HD. They were aimed at: (i) collecting sufficient numerical material for a quantitative discussion of effects of the asymmetric isotopic substitution, and (ii) providing an assessment of accuracy of new results for the Ar–HD(v

$=0,j=1$) complex (which cannot be verified at present by direct confrontation with experiment). Section III also contains a brief description of some preparatory tests which helped in choosing the input to the line-shape simulations of the Ar–HD absorption spectrum. Considered were: two empirical models of the induced-dipole moment, of Refs. 26 and 28, respectively, and two models of the intermolecular potential for Ar–H_2, the empirical XC model[17] and the theoretical (SAPT) potential.[16] In Sec. IV, a comprehensive presentation is made of results of the accurate close-coupling calculations performed on the absorption spectrum of the Ar–HD complex in this and previous works.[9] Factors determining the spectrum, energy level positions and widths, and relative intensities of individual transitions are analyzed and compared with the respective characteristics of the spectrum of Ar–H_2. An estimation of the changes introduced by asymmetry of the isotopic substitution is attempted. Besides the increase of the level widths, an effect of a decrease of the anisotropy relevant to the level positions (a decreased splitting of J levels) is estimated. A fragmentary estimation is also included of the (relatively small) impact of the asymmetric isotopic substitution on transition intensities. Line shapes of three bands of the Ar–HD spectrum, $S_1(1)$, $Q_1(1)$, and $Q_1(0)$, are presented. Predissociation effects occurring in the shapes of the first two bands are exposed by a comparison with the contours of the corresponding bands in the spectrum of Ar–H_2. Newly generated contours of the $S_1(1)$ and $Q_1(1)$ bands of the Ar–H_2 absorption spectrum are compared with recent experiment.[3] A number of new or more complete line assignments result from this comparison. In Sec. V, some general conclusions emerging from the present and previous[9] studies are stated.

II. THEORY

The absorption spectrum of the Ar–HD van der Waals complex can be viewed as a collection of resonance structures which appears in cross section for excess photoabsorption, caused by interaction between subunits of the complex, when the photon frequency is varied. Assuming that the Ar and HD subunits are in a low density gas mixture at thermal equilibrium, the cross-section σ is given by the following formula:[29]

$$\sigma(\omega)=\frac{4\pi^2\omega}{c}\sum_{\mathrm{i,f}} P_{\mathrm{i}}|\langle \mathrm{f}|\boldsymbol{\epsilon}\cdot\overline{\mathbf{d}}|\mathrm{i}\rangle|^2\delta(E_{\mathrm{f}}-E_{\mathrm{i}}-\hbar\omega), \qquad (1)$$

where ω and $\boldsymbol{\epsilon}$ denote the photon frequency and polarization, respectively, $\overline{\mathbf{d}}$ is the interaction-induced electric dipole moment of the complex, $|\mathrm{i}\rangle$ and $|\mathrm{f}\rangle$ stand for the initial and final rovibro-translational states of the complex respectively, E_{i} and E_{f} are energies of those states, and P_{i} is the population factor of the initial state at a given temperature T. Both the bound and free states of the complex are involved as initial states. Due to the conservation of energy, only free final states are possible when photon frequencies are within the near-infrared range. Thus, two kinds of transitions, bound–free and free–free, contribute to the absorption, so the cross section can be divided into two parts, $\sigma_{\mathrm{F}\leftarrow\mathrm{B}}$ and $\sigma_{\mathrm{F}\leftarrow\mathrm{F}}$, which are called the photodissociation and the CIA cross sections, respectively. Partial-wave expansion of the free (i.e., stationary scattering) states and application of the Wigner–Eckart theorem leads to the following expression for the CIA cross section:[9,18–20]

$$\sigma_{\mathrm{F}\leftarrow\mathrm{F}}(\omega)=\frac{4\pi^2\omega}{3c}\int dE_{\mathrm{i}}\,P(E_{\mathrm{i}}) \times\sum_{J_{\mathrm{i}}p_{\mathrm{i}}}\sum_{J_{\mathrm{f}}=|J_{\mathrm{i}}-1|}^{J_{\mathrm{i}}+1}\mathrm{Tr}\,\mathbf{T}^{\dagger}_{\mathrm{F}\leftarrow\mathrm{F}}\mathbf{T}_{\mathrm{F}\leftarrow\mathrm{F}}(\omega;J_{\mathrm{f}}J_{\mathrm{i}}p_{\mathrm{i}}E_{\mathrm{i}}), \qquad (2)$$

in which $\mathbf{T}_{\mathrm{F}\rightarrow\mathrm{F}}(\omega;J_{\mathrm{f}}J_{\mathrm{i}}p_{\mathrm{i}}E_{\mathrm{i}})$ denotes $N^o_{\mathrm{f}}\times N^o_{\mathrm{i}}$ matrix of reduced free–free phototransitions amplitudes

$$(\mathbf{T}_{\mathrm{F}\leftarrow\mathrm{F}})_{\gamma_k,\gamma_s}:=\langle E^-_{\mathrm{f}}J_{\mathrm{f}}p_{\mathrm{f}},\gamma_k\|\overline{\mathbf{d}}\|E^+_{\mathrm{i}}J_{\mathrm{i}}p_{\mathrm{i}},\gamma_s\rangle := \sqrt{2J_{\mathrm{f}}+1}\frac{\langle E^-_{\mathrm{f}}J_{\mathrm{f}}M_{\mathrm{f}}p_{\mathrm{f}},\gamma_k|\overline{d_q}|E^+_{\mathrm{i}}J_{\mathrm{i}}M_{\mathrm{i}}p_{\mathrm{i}},\gamma_s\rangle}{C(J_{\mathrm{i}}1J_{\mathrm{f}},M_{\mathrm{i}}qM_{\mathrm{f}})},$$

with $E_{\mathrm{f}}=E_{\mathrm{i}}+\hbar\omega$ and $p_{\mathrm{f}}=(-1)^{J_{\mathrm{f}}+J_{\mathrm{i}}+1}p_{\mathrm{i}}$; J, M, and p are the usual total angular momentum and the spectroscopic parity quantum numbers characterizing particular partial waves of the initial and final states; γ indicates the state of the Ar+HD system at infinite separation of the subunits from which a given ingoing ($|E^-\ldots\rangle$) or outgoing ($|E^+\ldots\rangle$) partial wave has evolved, i.e., three quantum numbers: vibrational (v) and rotational (j) of HD, and rotational (l) of Ar and HD about each other are collected in γ; N^o is the number of different γ's possible for the given E, J, and p, consistent with angular momentum addition rules and with the requirement that the (v,j)-state (of energy $\epsilon_{v,j}$) be an open scattering channel, $\epsilon_{v,j}<E$; $\overline{d_q}$ denotes component of the vector $\overline{\mathbf{d}}$ in the spherical basis and $C(\ldots)$ is the Clebsch–Gordan coefficient. In the analogous expression for the photodissociation cross section, N^o_{f}-dim. vector $\mathbf{T}_{\mathrm{F}\leftarrow\mathrm{B}}(\omega;J_{\mathrm{f}}J_{\mathrm{i}}p_{\mathrm{i}}n_iE^{\mathrm{B}}_i)$ with elements $(\mathbf{T}_{\mathrm{F}\leftarrow\mathrm{B}})_{\gamma_k}:=\langle E^-_{\mathrm{f}}J_{\mathrm{f}}p_{\mathrm{f}},\gamma_k\|\overline{\mathbf{d}}\|(E^{\mathrm{B}}Jpn)_i\rangle$ appears, where n is the van der Waals stretching or intermolecular vibration quantum number of Ar–HD. Since the values of E, J, and p are definite in bound states, the single sum $\Sigma_iP(E^{\mathrm{B}}_i)$ stands in place of the operations $\int dE_{\mathrm{i}}P(E_{\mathrm{i}})\Sigma_{J_{\mathrm{i}}p_{\mathrm{i}}}$. For convenience of reference, the formula for $\sigma_{\mathrm{F}\leftarrow\mathrm{F}}$ can be described as a sum of thermally averaged partial cross sections

$$\sigma_{\mathrm{F}\leftarrow\mathrm{F}}(\omega):=\sum_{J_{\mathrm{i}}p_{\mathrm{i}}}\sum_{J_{\mathrm{f}}}\tilde{\sigma}_{\mathrm{F}\leftarrow\mathrm{F}}(\omega;J_{\mathrm{f}}J_{\mathrm{i}}p_{\mathrm{i}}), \qquad (3)$$

and analogously, $\sigma_{\mathrm{F}\leftarrow\mathrm{B}}(\omega):=\Sigma_i\Sigma_{J_{\mathrm{f}}}\tilde{\sigma}_{\mathrm{F}\leftarrow\mathrm{B}}(\omega;J_{\mathrm{f}}J_ip_in_i)$.

The structures in the photoabsorption cross section are the manifestation of a temporal confinement of a colliding Ar+HD pair. Such a confinement, a metastable state of the Ar–HD complex, shows up as a rapid change in character of some free partial state(s) $|EJMp,\gamma_k\rangle$ (for $k=1,\ldots,N^o$) within a small energy range ($\sim 2\Gamma$) around E^{res}. The most pronounced variation is exhibited by the dominant component(s) of the function(s) of this state, to which some v, j, l, and n quantum numbers can be assigned (the same for all γ's). These numbers, denoted $(\overline{v},\overline{J},\overline{l}):=\overline{\gamma}$ and $\overline{n}$, give an approximate description of all the intra- and intermolecular vibrational and rotational modes of motion within the temporarily confined system; together with J they serve as labels

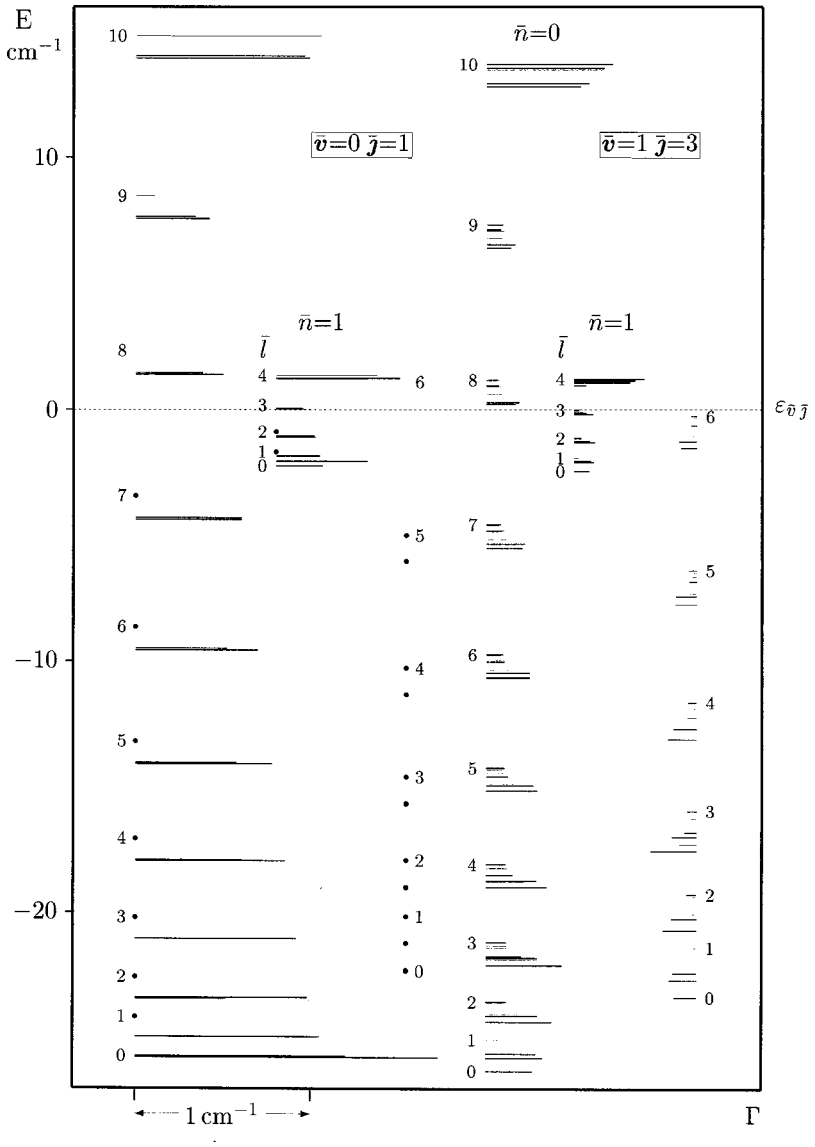

FIG. 1. Energy levels of Ar–HD: ($\bar{v}=0,\bar{J}=1,\bar{n}=0,1,\bar{l},J$) and ($\bar{v}=1,\bar{J}=3,\bar{n}=0,1,\bar{l},J$), and energy levels of Ar–H_2: ($\bar{v}=0,\bar{J}=1,n=0,\bar{l},J$) and ($\bar{v}=1,\bar{J}=3,\bar{n}=0,\bar{l},J$) (dots and lines with $\bar{l}$ labels standing on their right-hand sides). The energies are given relative to their respective dissociation thresholds: $\varepsilon_{0,1}=89.228\ \mathrm{cm}^{-1}$ and $\varepsilon_{1,3}=4141.424\ \mathrm{cm}^{-1}$—for Ar–HD and $\varepsilon_{0,1}=118.486\ \mathrm{cm}^{-1}$ and $\varepsilon_{1,3}=4831.392\ \mathrm{cm}^{-1}$—for Ar–$H_2$ ($\varepsilon_{0,0}=0$). The lengths of lines represent level widths. The widths for Ar–H_2 are multiplied here by 25. Dots denote bound state levels. The lower dots in the pairs below the ($\bar{v}=0,\bar{J}=1$) threshold of Ar–H_2 denote actually two close *e*-levels; the levels with $J=\bar{l}+1$ lie slightly above the $J=\bar{l}-1$ ones. Of the four "ladders" of levels drawn for the Ar–HD complex, the $\bar{n}=0$ ladders associated with the two ($\bar{v},\bar{J}$) thresholds, (0,1) and (1,3), consist of all ($\bar{l},J$) levels with $\bar{l}=0-10$, i.e., of 31 and 65 levels, respectively.

of metastable states of the Ar–HD complex. A metastable state with the $\bar{v}$ and $\bar{J}$ labels corresponding to a closed channel at E^{res} (i.e., $\epsilon_{\bar{v},\bar{J}}>E^{\mathrm{res}}$) is a predissociating state or Feshbach resonance. Obviously, the labeling of metastable states of the Ar–HD complex reflects the character of the interaction between the subunits—weak-anisotropy case[27]—and remains adequate also for bound states (except $\bar{n}$ goes over to the exact quantum number n).

The bound and metastable states of the Ar–HD complex are grouped $\bar{v}\{\bar{J}\{\bar{n}\{\bar{l}\{J\}\}\}\}$, where the spacing between the groups $\bar{v}\{\}$ for $\bar{v}=0,1$ corresponds to the vibrational energy quanta of HD, that between the (sub)groups $\bar{J}\{\}$ for $\bar{J}=0,1,\ldots$ etc. to the $\epsilon_{\bar{v}\bar{J}+1}-\epsilon_{\bar{v}\bar{J}}$ differences; two orders of magnitude smaller than the former and the latter are, respectively, the spacings between the $\bar{n}\{\}$ groups for $\bar{n}=0,1$ and the spacings between the subsequent $\bar{l}\{\}$ groups; the smallest (less than $1\ \mathrm{cm}^{-1}$) is the splitting of levels $J=|\bar{J}-\bar{l}|\cdots\bar{J}+\bar{l}$ within group with fixed $\bar{l}$, $\bar{J}$, $\bar{n}$, and $\bar{v}$. There are 20 truly bound state levels of Ar–HD.[9] Of interest here are the ones belonging to the $\bar{v}=0\bar{J}=1$ group which are the *f* levels, $p=(-1)^{\bar{J}+\bar{l}+J}=-1$, with $n=0$ and $\bar{l}=1-7$ and with $n=1$ and $\bar{l}=1,2$; cf. Fig. 1.

When $E_{\mathrm{i}}\approx E_{\mathrm{i}}^{\mathrm{res}}$ and $\hbar\omega\approx E_{f}^{\mathrm{res}}-E_{\mathrm{i}}^{\mathrm{res}}:=\Delta E_{\mathrm{fi}}^{\bar{}}$, the matrix $\mathbf{T}_{\mathrm{F}\leftarrow\mathrm{F}}(\omega;J_{\mathrm{f}}J_{i}p_{i}E_{\mathrm{i}})$ describes transition between metastable states, $|\bar{\mathrm{f}}\rangle\leftarrow|\bar{\mathrm{i}}\rangle$, where $\bar{\mathrm{i}}:=(\bar{\gamma}_{\mathrm{i}}\bar{n}_{\mathrm{i}}J_{\mathrm{i}})$ and $\bar{\mathrm{f}}:=(\bar{\gamma}_{\mathrm{f}}\bar{n}_{\mathrm{f}}J_{\mathrm{f}})$. Analogously, the vector $\mathbf{T}_{\mathrm{F}\leftarrow\mathrm{B}}(\omega;J_{\mathrm{f}}J_{i}p_{i}n_{i}E_{i}^{\mathrm{B}})$ describes transition from bound to metastable state when $\hbar\omega\approx E_{\mathrm{f}}^{\mathrm{res}}-E_{\mathrm{i}}^{\mathrm{B}}$ and $\bar{\mathrm{i}}=(\bar{\gamma}_{i}n_{i}J_{i})$. The strength of the transitions depends on the factors

$$(\mathbf{T}_{\mathrm{F}\leftarrow\mathrm{F}})_{\gamma_k,\gamma_s}\approx\langle F_{\bar{\gamma}_{\mathrm{f}}}^{(-)J_{\mathrm{f}}p_{\mathrm{f}}}(E_{\mathrm{f}}^{\mathrm{res}}\gamma_k;R)|D_{\bar{\gamma}_{\mathrm{f}},\bar{\gamma}_{\mathrm{i}}}\times(J_{\mathrm{f}}p_{\mathrm{f}}J_{\mathrm{i}}p_{\mathrm{i}};R)|F_{\bar{\gamma}_{\mathrm{i}}}^{(+)J_{\mathrm{i}}p_{\mathrm{i}}}(E_{\mathrm{i}}^{\mathrm{res}}\gamma_s;R)\rangle,\quad(4)$$

where

$$D_{\bar{\gamma}_{\mathrm{f}},\bar{\gamma}_{\mathrm{i}}}(J_{\mathrm{f}}p_{\mathrm{f}}J_{\mathrm{i}}p_{\mathrm{i}};R)=\sum_{L\Lambda}\langle\chi_{\bar{v}_{\mathrm{f}}\bar{J}_{\mathrm{f}}}(r)|\bar{d}_{L\Lambda}(r,R)|\chi_{\bar{v}_{\mathrm{i}}\bar{J}_{\mathrm{i}}}(r)\rangle_r\langle\overline{J_{\mathrm{f}}l_{\mathrm{f}}}J_{\mathrm{f}}\|\mathcal{Y}_{L\Lambda}^{1}\|\overline{J_{\mathrm{i}}l_{\mathrm{i}}}J_{\mathrm{i}}\rangle,$$

$$\langle \overline{J_f l_f} J_f \| \mathcal{Y}^1_{L\Lambda} \| \overline{J_i l_i} J_i \rangle := \{[L][\Lambda][\overline{J_i}][\overline{l_i}][J_i] \times [J_f]\}^{1/2} C(\overline{J_i} L \overline{J_f}; 000) C(\overline{l_i} \Lambda \overline{l_f}; 000) \times \begin{Bmatrix} J_f & J_i & 1 \\ \overline{J_f} & \overline{J_i} & L \\ \overline{l_f} & \overline{l_i} & \Lambda \end{Bmatrix},$$

$[L] := 2L+1$, in which: (i) the Jacobi coordinates in the space-fixed reference frame are $\mathbf{r} := (r, \hat{\mathbf{r}}), \mathbf{R} := (R, \hat{\mathbf{R}})$, the lengths and spherical angles of the vectors which point from H to D and from the center of mass of HD to Ar, respectively; (ii) the close-coupling expansion of the partial waves is $\langle \mathbf{r}, \mathbf{R} | E^{\pm} JMp, \gamma \rangle = (1/R)\, \mathbf{\Phi}^{JMp}(\mathbf{r}, \hat{\mathbf{R}}) \mathbf{F}^{(\pm)Jp}(E, \gamma; R)$, where the basis $\mathbf{\Phi}^{JMp}(\mathbf{r}, \hat{\mathbf{R}}) := \{(1/r)\, \chi_{(vj)_k}(r) \mathcal{Y}^{JMp}_{(jl)_k}(\hat{\mathbf{r}}, \hat{\mathbf{R}})\}_{k=1}^{N}$ is built of rovibrational radial functions of HD, $\chi_{vj}(r)$, and of eigenfunctions of the angular momentum operators, $\hat{\mathbf{j}}^2$, $\hat{\mathbf{l}}^2$, $\hat{\mathbf{J}}^2 := (\hat{\mathbf{j}} + \hat{\mathbf{l}})^2$, and $\hat{J}_z$, having definite spectroscopic parity, $p = 1$ or $p = -1$; (iii) the expansion of the induced-dipole moment functions in the angular basis is $\overline{d}_q(\mathbf{r}, \mathbf{R}) = (4\pi/\sqrt{3}) \Sigma_{L\Lambda} \overline{d}_{L\Lambda}(r, R) \mathcal{Y}^{1q1}_{L\Lambda}(\hat{\mathbf{r}}, \hat{\mathbf{R}})$. The approximate character of Eq. (4) for $(\mathbf{T}_{F \leftarrow F})_{\gamma_k, \gamma_s}$ lies in that only the dominant components of the respective vectors of the radial functions $\mathbf{F}^{(-)J_f p_f}(E^{\mathrm{res}}_{\overline{f}}, \gamma_k; R)$ and $\mathbf{F}^{(+)J_i p_i}(E^{\mathrm{res}}_{\overline{i}}, \gamma_s; R)$ are retained. An analogous approximate formula for $(\mathbf{T}_{F \leftarrow B})_{\gamma_k}$, with the dominant component of the vector $\mathbf{F}^{(B)J_i p_i}(E^B_i; R))$ standing in place of $F^{(+)J_i p_i}_{\overline{\gamma}_i}(E^{\mathrm{res}}_{\overline{i}} \gamma_s; R)$, can be used for an estimation of the strength of bound–free transitions. (Obviously, such crude formulas cannot be used in any calculations called "accurate.") From the structure of the formula for $D_{\overline{\gamma}_f, \overline{\gamma}_i}(J_f p_f J_i p_i; R)$, which is the respective (reduced) matrix element of the dipole operator in the basis $\mathbf{\Phi}^{JMp}(\mathbf{r}, \hat{\mathbf{R}})$, the selection rules for transitions in the complex are inferred.[26,30,31] The strict ones, concerning J and p, have already been indicated in Eq. (2); they result solely from the properties of the rotational factors $\langle \| \mathcal{Y}^1_{L\Lambda} \| \rangle$. The rules for the approximately preserved quantum numbers $\overline{J}$ and $\overline{l}$ result from dominance of some radial components $\overline{d}_{L\Lambda}(r, R)$ in the dipole moment function, namely, those with $(L, \Lambda) = (2,3)$ and $(0,1)$, and are: $\Delta\overline{J} = 0, \pm 2$ and $\Delta\overline{l} = \pm 3, \pm 1$. The notation used for transitions $\overline{f} \leftarrow \overline{i}$ allowed by the selection rules and for groups of these transitions distinguished by transition energy, $\Delta E_{\overline{fi}}$, is summarized in Table I. Transitions comprising the $Q_1(1)$ and $S_1(1)$ bands are presented schematically in Fig. 2.

Summarizing, there are three basic factors determining the absorption spectrum of the complex: the pattern of energy levels of bound and metastable states, the decay rates of the metastable states, and the intensities of individual transitions between the states. The first two factors depend sensitively on the intermolecular potential of the complex, $\overline{V}(\mathbf{r}, \mathbf{R})$, and the third involves additionally the induced-dipole moment, $\overline{\mathbf{d}}(\mathbf{r}, \mathbf{R})$. Since both these quantities do not depend on nuclear masses, within the clamped nuclei version of the Born–Oppenheimer approximation, they are obtained from the respective functions for the Ar–H_2 complex, $V(\mathbf{r}, \mathbf{R}_{Ar-H_2})$ and $\mathbf{d}(\mathbf{r}, \mathbf{R}_{Ar-H_2})$, by simple coordinate transformation, $\overline{V}(\mathbf{r}, \mathbf{R}) = V(\mathbf{r}, \mathbf{R} + f\mathbf{r})$, where $f\mathbf{r}$ with $f = [m_D/(m_H + m_D)] - \frac{1}{2}$ is the displacement of the center of mass of HD

TABLE I. Transitions $(\overline{v_f} \overline{J_f} \overline{n_f} \overline{l_f} J_f) \leftarrow (\overline{v_i} = 0 \overline{J_i} \overline{n_i} \overline{l_i} J_i)$ in weak-anisotropy complexes. Notation.

Group	Numbers specified[a]	Notation		
Band	$\overline{v_f}, \overline{J_i}, \Delta\overline{J}$	$B_{\overline{v_f}}(\overline{J_i})$	$B := Q, S$	for $\Delta\overline{J} = 0, +2$
Subband	$\overline{n_i}, \overline{n_f}$	$n = \overline{n_f} \leftarrow \overline{n_i}$		
Branch	$\Delta\overline{l}$	b	$b := T, R, P, N$	for $\Delta\overline{l} = +3, +1, -1, -3$
b-transition	$\overline{l_i}, \Delta\overline{l}$	$b(\overline{l_i})$		
Transition	$\overline{l_i}, J_i, \Delta\overline{l}, \Delta J$	$b_\alpha(\overline{l_i}, J_i)$	$\alpha := +, -, 0$	for $\Delta J = +1, -1, 0$

[a] $\Delta x := x_f - x_i$ for $x = \overline{J}, \overline{l}, J$.

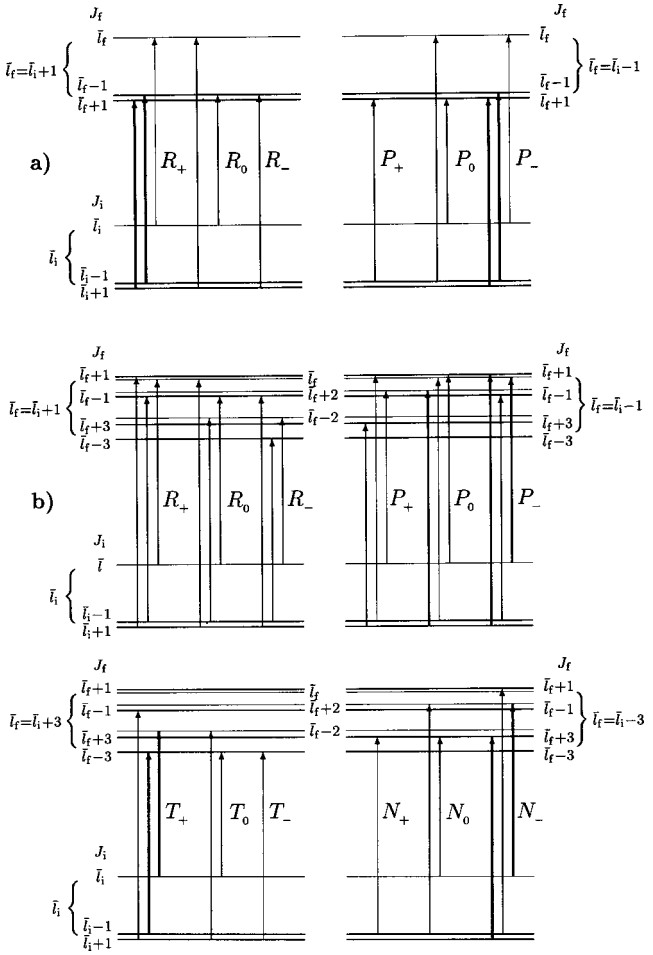

FIG. 2. (a) Components of $R(\overline{l_i})$- and $P(\overline{l_i})$ transitions in $Q_1(1)$ band. There are only single components of $T(\overline{l_i})$- and $N(\overline{l_i})$ transitions in this band: $T_+(\overline{l_i}, \overline{l_i}+1)$ and $N_-(\overline{l_i}, \overline{l_i}-1)$, respectively. (b) Transitions $(\overline{l_f} J_f) \leftarrow (\overline{l_i} J_i)$ in $S_1(1)$ band. The orderings of f levels (thinner lines) and of e levels within the initial and the final $\overline{l}\{\,\}$ groups are as typically occur in Ar–HD and in Ar–H_2 (except the relative position of $J_i = \overline{l_i}+1$- and $J_i = \overline{l_i}-1$ levels is reversed in the latter case); cf. Fig. 1. The thick (thin) arrows denote the most (the least) intense components of the transitions.

from the position in H_2. This operation naturally brings into consideration the question of what effects it introduces to the absorption spectrum of the complex.

In a qualitative analysis of *the effects of the asymmetric isotopic substitution in the absorption spectrum of the Ar–HD complex* one may concentrate only on those introduced via the intermolecular potential; the changes of the total intensities of transitions caused by the transformation of the dipole moment function (being not large, cf. Sec. IV) do not have any dramatic impact on the spectrum shape. The contribution to the intermolecular potential generated by the isotopic substitution, $v(\mathbf{r},\mathbf{R}) \equiv \overline{V}(\mathbf{r},\mathbf{R}) - V(\mathbf{r},\mathbf{R})$, and its implications for energy level positions and predissociation rates are a well-analyzed subject.[4,5] Essential is the anisotropy character of $v(\mathbf{r},\mathbf{R})$, i.e., the difference between expansions of the potentials $\overline{V}(\mathbf{r},\mathbf{R})$ and $V(\mathbf{r},\mathbf{R})$ into Legendre polynomials, $P_L(\cos(\hat{\mathbf{r}}\cdot\hat{\mathbf{R}}))$ for $L=0,1,\ldots$, where L is the polynomial order. The strength of the particular terms occurring in these expansions is determined by the respective radial functions, $\overline{V}_L(r,R)$ and $V_L(r,R)$. Thus, the differences, $\overline{V}_L(r,R) - V_L(r,R) \equiv v_L(r,R)$, are the isotopic corrections to the Lth order anisotropy strength functions. The facts established are: (i) the corrections to even-order anisotropy affect mostly the positions of energy levels: v_0 shifts the entire groups $\overline{l}\{\}$ and v_2 changes the splitting within the groups; (ii) the appearance of first-order anisotropy term in $\overline{V}$, $\overline{V}_1 = v_1$, enhances greatly the rotational predissociation: for all states $(\overline{v},\overline{J},\overline{n},\overline{l},J)$ labeled with $\overline{J} \geqslant 2$ and for $p=1$-parity states (e-levels) with $\overline{J}=1$ it becomes possible to decay into energetically closest dissociation channels, associated with the respective $\varepsilon_{\overline{v},\overline{J}-1}$ thresholds. Obviously, the increase of decay rates is most dramatic for the latter states, since in Ar–H_2 they can decay only to the distant $(\overline{v}-1,j)$ channels or (for $\overline{v}=0$) are bound. The differences between predissociation governed by the $L=1$ and by the $L=2$ anisotropy of the potential can be stated in the form of some approximate selection rules for the underlying bound–continuum transitions. To this end the following (simplified) perturbative formula for Γ should be recalled:

$$\Gamma_{\overline{v}J\overline{n}\overline{l}J} \approx 2\pi \sum_{jl} |\langle \overline{J}\,\overline{l}J|P_L|jlJ\rangle \times \langle \widetilde{F}^{(B)}_{\overline{v}J\overline{n}\overline{l}J}|\langle \chi_{\overline{v}\overline{l}}|V_L|\chi_{\overline{v}j}\rangle_r|\widetilde{F}^{(+)J}_{vjl}\rangle_R|^2, \quad (5)$$

where $\widetilde{F}^{(B)}_{\overline{v}J\overline{n}\overline{l}J}(R)$ denotes the radial function of a bound state giving zeroth-order approximation to the predissociating state and $\widetilde{F}^{(+)J}_{vjl}(R)$ is a one-channel scattering function at $E \approx E^{\mathrm{res}}_{\overline{v}J\overline{n}\overline{l}J}$, in which the mixing of l components has been neglected. The rules are: $\overline{J}-j=L$ and $\overline{l}-l=\pm 1$ when $L=1$, and $\overline{l}-l=\pm 2,0$ when $L=2$.

As to the implications of the isotopic corrections (to the potential) on the spectrum shape, at least two categories of effects can be distinguished. Besides the primary effects to which obviously belong broadening (strictly, flattening) of lines and shifts in lines positions, some secondary effects of the broadening may appear important, such as ''appearance'' or ''disappearance'' of some transitions from spectrum contour, accumulation of intensity of neighboring broad lines, and shifts of line centers due to the accumulation. All these secondary predissociation effects are evidently mediated by the induced-dipole moment. An example of a secondary predissociation effect can be found in the $S_1(0)$ band of Ar–HD when one compares it with the corresponding band of Ar–H_2 (Figs. 11 and 3, respectively, of Ref. 3). Whereas in the latter spectrum the heights of N lines tend to increase when going from the band center towards its edge, the opposite tendency is revealed in the former. Accumulation of intensity of transitions from relatively rapidly decaying quasibound (tunneling) states has been ascertained in a recent study[9] to be the cause of the reversal. Evidence has been given thereby that transitions producing lines too diffuse to have noticeable impact on the shape of the sharp absorption spectrum of Ar–H_2 may acquire some importance in the flattened spectrum of Ar–HD. Much stronger effects of the same kind can be expected in the $Q_1(1)$ and $S_1(1)$ bands of Ar–HD for the reason that the broadening of lines produced by different transitions in these bands is certainly less uniform. Generally, lines of transitions from the predissociating $p=1$-parity states $(\overline{v}=0,\overline{J}=1,\overline{l},J=\overline{l}\pm 1)$ will be broadened much more than lines of transitions from the bound $p=-1$-parity states $(J=\overline{l})$. Thus, relative heights of lines of the two kinds may be significantly altered in comparison with their counterparts in the spectrum of Ar–H_2.

III. CALCULATIONS

As follows from the Introduction, the calculations on the photoabsorption dynamics of the Ar–HD complex planned to be performed in this work have mainly a predictive character. Associated with this was the need for performing some additional tests which would provide an estimation of the accuracy of the new results. Such information is desirable because the input used in the calculations, the XC fit to the intermolecular potential of Ar–H_2[17] and the Dunker–Gordon model of the induced-dipole moment,[26] though the best available, is not yet fully reliable in all respects which matter in the description of Ar–HD.

A. Testing the input

The Dunker–Gordon model of the induced-dipole moment may indeed be a source of uncertainty, cf. Refs. 7, 8, 28. Though the doubts raised are not essential for reproducing the experimental shape of the $S_1(0)$ band of Ar–HD, as it appeared in a recent study,[9] additional tests of the model were required before applying it to calculations on other bands. In particular, a comparison was made with the later model,[28] fitted to the improved experimental data of Ref. 2. The conclusions are: (i) the two models are almost indistinguishable when shapes of the $S_1(1)$ band of Ar–H_2 resulting from them are compared; (ii) in order to achieve similar consistency of results for the $Q_1(1)$ band of Ar–H_2, the radial part of the charge-induced component in the Dunker–Gordon model has to be strengthened by a factor of approximately 3.[32] Eventually, the Dunker–Gordon model was chosen for calculations on the corresponding bands of Ar–HD

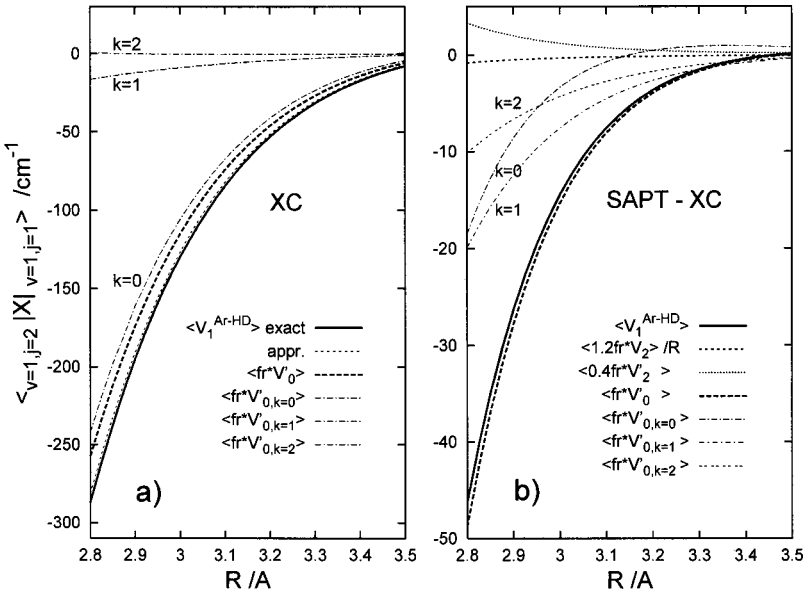

FIG. 3. (a) First-order anisotropy coupling element $\langle\chi_{12}|\overline{V}_1\chi_{11}\rangle_r$ with $\overline{V}_1$ determined from the XC potential, exactly and approximately: $\overline{V}_1^{\rm appr}=fr[V_0'+(2/5)V_2'+(6/5R)\,V_2]$, where prime denotes derivative with respect to R. [The sign of $\overline{V}_1$ differs from the sign in Eq. (15) of Ref. 4 because the opposite orientation of the vector $\mathbf{r}$ is assumed in this work]. Plotted are also: the element $\langle\chi_{12}|frV_0'\chi_{11}\rangle_r$ and the contributions to this element which arise from the expansion $V_0(R,r)=\Sigma_k V_{0,k}(R)(r/r_0-1)^k$, where r_0 is the mean separation of atoms in the $v=0,j=0$ state of H_2. (b) Deviations $\langle\chi_{12}|X^{\rm SAPT}-X^{\rm XC}|\chi_{11}\rangle_r$ for $X=\overline{V}_1^{\rm appr}$ and for the terms of $\overline{V}_1^{\rm appr}$ arising from the isotropic and the second-order anisotropy terms of V.

[with the d_{01} strength parameter multiplied by 3 for the $Q_1(1)$ band] because its functional form is better suited to the isotopic substitution transformation (explicit dependence on the r coordinate). The transformation was performed following the (accurate) procedure of Ref. 9.

The XC fit to the potential for Ar–H_2 is, indeed, the most reliable model to choose when the accuracy of transition energies is concerned. Unfortunately, that model seems to have a (small) defect in the repulsive wall region which affects accuracy of predissociation rates in Ar–HD. The widths of lines in the $S_1(0)$ band of Ar–HD resulting from the XC potential have been found in Ref. 9 to be too small and less consistent with experiment than the widths generated from the theoretical (SAPT) potential.[16] Believing that this finding can be extrapolated to other bands of Ar–HD, it was decided to calculate linewidths in the $S_1(1)$ and $Q_1(1)$ bands from both the XC and SAPT potentials. Additionally, some tests were carried out whose results may be helpful in correcting the short-range behavior of the XC fit.

Figure 3 presents an analysis of the differences between the $\overline{V}_1$ terms which result from the XC and SAPT potentials V. Strictly, the element $\langle\chi_{12}|\overline{V}_1\chi_{11}\rangle_r$ is analyzed which is the main factor determining the widths of lines in the $S_1(0)$ band of Ar–HD, cf. Eq. (5). The different derivatives $(\partial/\partial R)\,V_0(R,r)$ and, in particular, their different dependencies on the r coordinate in the SAPT and XC potentials, are shown to be the main source of the deviations $\langle\chi_{12}|\overline{V}_1^{\rm SAPT}-\overline{V}_1^{\rm XC}|\chi_{11}\rangle_r$ in the small R region. For $R<3.3$ Å, the contribution of $(\partial/\partial R)\,(V_0^{\rm SAPT}-V_0^{\rm XC})$ to the deviations exceeds more than 10 times the total contribution of the differences in the V_2 terms of the two potentials. Figure 4 summarizes some tests which were made in order to establish how sensitive the widths of the $(\overline{v}=1,\overline{J}=2,n=0,\overline{l},J=\overline{+}2)$ states of Ar–HD are to the strength and composition of the element $\langle\chi_{12}|\overline{V}_1\chi_{11}\rangle_r$. In these tests, the configuration-mixing (CM) theory[33] of resonances was exploited, in the version[34] one discrete state interacting with coupled continua. The curves marked with LT and CM in Fig. 4 serve to show that the approximate treatment of dynamics, pertinent to the CM theory, is adequate in the cases tested. The use of the approximate formula of Ref. 4 for the coupling $\langle\chi_{12}|\overline{V}_1\chi_{11}\rangle_r$, including only linear terms in the displacement parameter f, is shown to impair slightly the widths; the CM~ values are smaller by ca. 3% than the CM results. Finally, the comparison of the CM~ results with those denoted as CM~sph

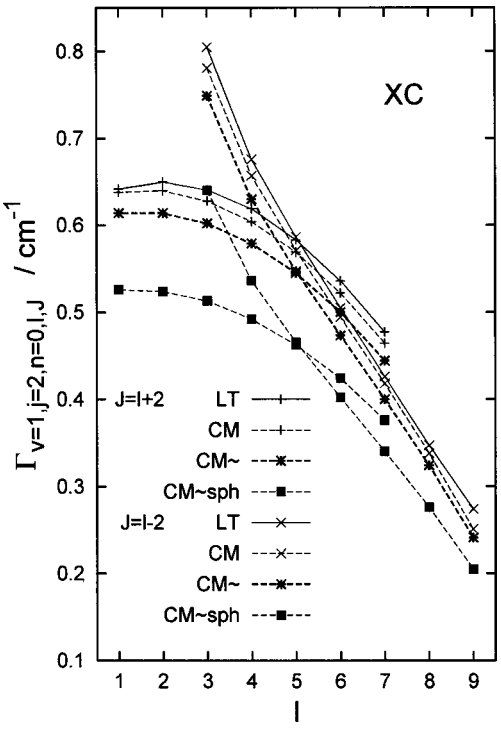

FIG. 4. Widths of $(\overline{v}=1,\overline{J}=2,\overline{l},J=\overline{l}\pm2)$ states of Ar–HD. LT—"exact" results (from Life-Time matrix analysis (Ref. 9), LT matrices evaluated using $\overline{V}^{\rm XC}$, the transformation $V^{\rm XC}\rightarrow\overline{V}^{\rm XC}$ performed numerically); CM—perturbative results (from configuration-mixing approach,[33,34] all couplings evaluated using exact $\overline{V}^{\rm XC}$). CM~ and CM~sph denote perturbative results obtained when the exact element $\langle\chi_{12}|\overline{V}_1^{\rm XC}\chi_{11}\rangle_r$ (only this one) was replaced with $\langle\chi_{12}|\overline{V}_1^{\rm XC\ appr}\chi_{11}\rangle_r$ [cf. Fig. 3(a)] and $\langle\chi_{12}|frV_0'^{\rm XC}\chi_{11}\rangle_r$, respectively.

TABLE II. Averaged partial cross sections, $\tilde{\sigma}_{\mathrm{Type}}(\omega;J_f J_i p_i n_i)$, determined in the line shape calculations for Ar–HD. The averaging was done at $T=77$ K with unnormalized Boltzmann factors: $\exp(-E_i^B/kT)$ and $\exp(-E_i/kT)/\Sigma_{j=0}^{j\ \mathrm{open}}(2j+1)\exp(-\varepsilon_{0j}/kT)$ for transitions from bound and from free states, respectively.

Band	Type	p_i	n_i	J_i	J_f-J_i	Number of $\tilde{\sigma}$'s	Aver. number of **T**'s per $\tilde{\sigma}$[a]
$Q_1(1)$	F←B	−1	0	1–8[b]	0	8	1000
		−1	1	1–3[b]	0	3	
	B←B[c]	−1	0	1–8[b]	±1, $J_f\leqslant 8$	14	1
	B←F[c]	1	-	1–8	0	11[d]	1000
	F←F	1	-	0–10	±1, $J_f\leqslant 10$	20	160×270
		−1	-	9–10	±1, 0, $J_f\leqslant 10$	5	
$S_1(1)$	F←B	−1	0	1–8[b]	±1, 0	23	2000
		−1	1	1–3[b]	±1, 0	8	
	F←F	1	-	0–11	±1, 0, $J_f\leqslant 10$	31	190×270
		−1	-	9–10	±1, 0, $J_f\leqslant 10$	5	

[a]The average numbers of individual transition amplitude matrices which were calculated to determine one partial cross section of given type as function of ω in the region 3605–3655 cm^{-1} for $Q_1(1)$ and 4030–4070 cm^{-1} for $S_1(1)$ band. In F←F cases, the number of **T**'s is shown as: the number of values of ω chosen to cover the respective region × the number of points necessary for integration over E_i. The integrations were done over the ranges 15–500 cm^{-1} for $Q_1(1)$ and 46–116 cm^{-1} for $S_1(1)$ band.

[b]The values $J_i=8$ and $J_i=3$ (for $n_i=1$) correspond to tunneling states lying above the $(\bar{v}=0,\bar{J}=1)$ threshold (cf. Fig. 1). Because of very small widths they were treated as bound states.

[c]This includes transitions to the states $(\bar{v}=1,\bar{J}=1,\bar{n}=0,\bar{l}=J=1-8)$ which are bound because of the representation chosen (see the text) or have very small width $(J=8)$.

[d]This includes three transitions to states with $n_f=1$ and $J_f=1-3$.

reveals that ~85% of the widths are due to the isotropic term of the potential V. This is a substantially higher contribution than that obtained in Ref. 5 (from one of the older empirical potentials for Ar–H_2).

Line-shape calculations of the absorption spectrum of Ar–HD were carried out in two steps. Determination of energies and widths of the bound and metastable states of the complex associated with three Ar+HD$(\bar{v},\bar{J})$ dissociation channel, $(\bar{v},\bar{J})=(0,1),(1,1)$, and (1,3), was the necessary first step. In view of the results presented in Ref. 9, only states associated with the highest threshold had to be determined in this work. This was done following the same procedures as used in Ref. 9 (isolated-resonance analysis of lifetime matrices obtained in convergent close-coupling calculations).

In the second step, the photoabsorption cross section of the complex

$$\sigma^{\mathrm{Ar-HD}}(\omega):=\sigma_{\mathrm{F\leftarrow B}}(\omega)+\sigma^{\mathrm{res}}_{\mathrm{F\leftarrow F}}(\omega), \tag{6}$$

was evaluated in two regions of ω (of width ~45 cm^{-1}) centered at the frequencies of the $Q_1(1)$ and $S_1(1)$ transitions in HD, 3628.305 and 4052.196 cm^{-1}, respectively. In the $\sigma^{\mathrm{res}}_{\mathrm{F\leftarrow F}}$ part, free–free partial cross sections $\tilde{\sigma}_{\mathrm{F\leftarrow F}}(\omega;J_f J_i p_i)$ [cf. Eq. (3)] were included which exhibit resonance structures in the regions of interest. The specification of all the partial cross sections included in the function $\sigma^{\mathrm{Ar-HD}}(\omega)$ to simulate the contours of the $Q_1(1)$ and $S_1(1)$ bands is given in Table II. From the information in the last two columns of this table, it should become evident that the bulk of the computational work associated with the simulations was devoted to the determination of the $\sigma^{\mathrm{res}}_{\mathrm{F\leftarrow F}}$ parts; the total number of evaluations of the $\mathbf{T}_{\mathrm{F\leftarrow F}}$ matrices exceeded more than 30 times the total number of evaluations of the $\mathbf{T}_{\mathrm{F\leftarrow B}}$ vectors.

The initial and final states of Ar+HD involved in the transition amplitudes were represented in the bases $\mathbf{\Phi}^{JM_P}(\mathbf{r},\hat{\mathbf{R}})$ in which rovibrational functions of HD with fixed v number were used: $v=0$ for the initial and $v=1$ for the final states. The values of j ranged from $j_{\min}=0(1)$ for the $p=1(-1)$ -parity states to $j_{\max}=2$ for the initial states, and $j_{\max}=2$ and 4—for the final states in the $Q_1(1)$ and in the $S_1(1)$ bands, respectively. Thus, the respective maximal dimensions of the sets of coupled radial equations dealt with in the evaluation of the transitions amplitudes were: $N_i=6$, $N_f=6$ and 15. The method of solving the coupled equations and the accuracy parameters were described in Ref. 9.

Another fact to note in Table II is the appearance of the partial cross sections of free–bound and bound–bound types, needed in the simulation of the $Q_1(1)$ band. This is obviously a consequence of the representation chosen; the metastable states of the complex which can decay only by vibrational predissociation show up as bound states. In order to add contributions from the bound–bound transitions to the function $\sigma^{\mathrm{Ar-HD}}(\omega)$, the calculated total intensities of these transitions were convoluted with Gaussians of width 0.08 cm^{-1} (the experimental resolution taken from Table I of Ref. 3).

Line-shape simulations of the $Q_1(1)$ and $S_1(1)$ bands *of the* Ar–H_2 *absorption spectrum* were made with the help of the function

$$\sigma^{\mathrm{Ar-H_2}}(\omega):=\sum_{f\leftarrow i}\int_{-\infty}^{+\infty}G(\omega-\omega')\sigma_{\bar{f}\leftarrow\bar{i}}(\omega')d\omega', \tag{7}$$

where $\sigma_{\bar{f}\leftarrow\bar{i}}(\omega)$ denotes profile, a Lorentzian or a δ-type profile, of individual N-, T-, R-, or P transition between metastable and bound states of the complex, and $G(\omega)$ is a Gaussian, $G(\omega)=(a/\sqrt{\pi})\exp(-a^2\omega^2)$, with full width at half maximum FWHM$=2\sqrt{\ln 2}/a$ set equal to the experimental resolution[3] of 0.04 cm^{-1}. The list of the $\sigma_{\bar{f}\leftarrow\bar{i}}(\omega)$ profiles included in the function $\sigma^{\mathrm{Ar-H_2}}(\omega)$, together with some details on calculations of the parameters of the profiles (positions, maximal intensities and widths), are given in Table III. The last column of this table summarizes information on widths of the profiles. This shows that the widths due to rotational predissociation of the majority of profiles in the $S_1(1)$ band are on average one order of magnitude smaller than the resolution achieved in this region in the recent experiment. Thus, predissociation effects, especially the secondary ones, are practically absent in the function $\sigma^{\mathrm{Ar-H_2}}(\omega)$; for both the $S_1(1)$ and the $Q_1(1)$ bands the heights of peaks in this function reflect essentially relative intensities of individual transitions contributing to the bands. Obviously, strong effects of intensity accumulation can occur when energies of the transitions coincide within the experimental resolution.

TABLE III. Profiles $\sigma_{\bar{f}\leftarrow\bar{i}}(\omega)$ of transitions $(\bar{v}_f\bar{J}_f\bar{n}_f=0\bar{l}_fJ_f)\leftarrow(\bar{v}_i=0\bar{J}_i\bar{n}_i=0\bar{l}_iJ_i)$ determined in the spectrum shape calculations for Ar–H_2.

Band	Type of transitions[a]	$\bar{l}_i$	$\bar{l}_f$	Number of profiles[b]	Average widths[c]
$Q_1(1)$	B←B	0–6[d]	0–6[e]	74	0
	F←B	4,6[d]	7	7	0.09
	B←F	7	4,6[e]	7	0.21
$S_1(1)$	F←B	0–6[d]	0–6	128	0.003
	F←B	4,6[d]	7	15	0.076
	F←F	7	4,6	15	0.21

[a]For transitions $\bar{f}\leftarrow\bar{i}$ of type=F←B, B←F, and F←F, the profiles were taken as Lorentzians, $\sigma_{\bar{f}\leftarrow\bar{i}}(\omega)=\tilde{\sigma}_{\text{Type}}(\omega_{\bar{f}\bar{i}})/[1+4\hbar^2(\omega-\omega_{\bar{f}\bar{i}})^2/\Gamma^2_{\text{Type}}]$, with $\Gamma_{\text{Type}}=\Gamma_f,\Gamma_i,\Gamma_f+\Gamma_i$, respectively, and for B←B transitions, $\sigma_{\bar{f}\leftarrow\bar{i}}(\omega)=\tilde{\sigma}_{\text{B}\leftarrow\text{B}}(\omega_{\bar{f}\bar{i}})\delta(\omega-\omega_{\bar{f}\bar{i}})$; $\hbar\omega_{\bar{f}\bar{i}}$ is the transition energy and $\tilde{\sigma}_{\text{Type}}(\omega_{\bar{f}\bar{i}})$ denotes the corresponding maximum in the thermally averaged partial cross section $\tilde{\sigma}_{\text{type}}(\omega;J_fJ_ip_in_i=0)$, cf. Eq. (3).

[b]The parameters of the profiles, $\omega_{\bar{f}\bar{i}}$, Γ, and $\tilde{\sigma}(\omega_{\bar{f}\bar{i}})$, were determined in the close-coupling calculations in which rigid rotator type bases, $\mathbf{\Phi}^{JMp}(\mathbf{r},\hat{\mathbf{R}})=\{(1/r)\chi_{\bar{v}\bar{J}}(r)\mathcal{Y}^{JMp}_{jl}(\hat{\mathbf{r}},\hat{\mathbf{R}});\ j=1,3,5\}$, were used to represent states of the Ar–$H_2(\bar{v},\bar{J})$ complex with $(\bar{v},\bar{J})=(0,1),(1,1),(1,3)$. Rovibrational energies of H_2 were approximated as $\varepsilon_{\bar{v}j}\approx\varepsilon_{\bar{v}0}+B_{\bar{v}}(\bar{J})j(j+1)$ with $B_{\bar{v}}(\bar{J})$ chosen to give the exact values of $\varepsilon_{\bar{v}\bar{J}}$ (listed in footnote b to Table V). In calculations of maxima of the profiles, $\tilde{\sigma}(\omega_{\bar{f}\bar{i}})$, Boltzmann factors of the form $P(E_i)=\exp(-(E_i-\varepsilon_{01})/kT)$ with $T=77$ K were used for all types of $\bar{f}\leftarrow\bar{i}$ transitions.

[c]The widths of the profiles are given in cm^{-1}.

[d]Initial states with $\bar{l}_i=6$ are actually tunneling states of very small widths (cf. Fig. 1).

[e]These states are bound because of the neglect of vibrational predissociation. The state $\bar{l}_f=J_f=6$, of energy above ε_{11}, has very small width.

IV. DISCUSSION OF RESULTS

A. Energy levels: Positions and widths

Energies and widths of the $(\bar{v},\bar{J},\bar{n},\bar{l},J)$ states of the Ar–HD and Ar–H_2 complexes associated with two $(\bar{v},\bar{J})$ thresholds of interest in this work, (0,1) and (1,3), are presented schematically in Fig. 1. As to the positions of the energy levels, the major effect of asymmetry of the isotopic substitution seen in this figure is the decreased splitting of J levels within the $\bar{l}\{\}$ groups in the Ar–HD complex. The decrease is of the order of 20%–30% and arises mainly from the fact that the strength function of the second-order anisotropy term of the intermolecular potential, $V_2(r,R)$ (cf. Fig. 4 in Ref. 17), and the isotopic correction to it, $v_2(r,R)$, have opposite signs for Rs in the van der Waals well region; cf. Eq. (16) and Fig. 2 of Ref. 4.

The crucial role of asymmetry of the isotopic substitution in causing the decreased splitting of J levels in the Ar–HD complex is exhibited in Table IV. The splitting in the Ar–H_2, Ar–HD, and Ar–D_2 complexes is compared in this table on two representative $\bar{v}=1\bar{J}=2n=0\bar{l}\{\}$ groups. Two kinds of results for Ar–HD are included : the exact ones (from the potential $\bar{V}$) and results generated from the untransformed potential $(f=0)$. The comparison reveals a tendency of the splitting to grow with the mass of the diatomic subunit. The splitting in Ar–HD is shown to change substantially (becoming larger than in Ar–H_2) when asymmetry of this complex is ignored. Columns 5 and 6 of Table IV list results of some auxiliary tests which allow for a direct estimation of the contribution of the v_2 correction to the splitting of J levels in Ar–HD. In the two cases shown, this contribution is even larger than 30% of the splitting due to the V_2 term of the potential.

TABLE IV. Splitting of levels within two representative $\bar{v}=1\bar{J}=2n=0\bar{l}\{\}$ groups in the Ar–H_2, Ar–HD, and Ar–D_2 complexes, $\Delta E=E(J=\bar{l})-E(J=\bar{l}-2)$.

	Ar–H_2	Ar–HD				Ar–D_2
$\bar{l}$	ΔE	ΔE	$\Delta E(f=0)$[a]	$\Delta E^{(1)}$[b]	$\Delta E^{(1)}(f=0)$[c]	ΔE
3	1.337	0.79	1.48	0.80	1.35	1.543
6	1.139	0.84	1.29	0.88	1.28	1.325

[a]Results from untransformed potential.

[b]Perturbative results, $\Delta E^{(1)}=[\langle\overline{JlJ}=\bar{l}|P_{L=2}|\overline{JlJ}=\bar{l}\rangle-\langle\overline{JlJ}=\bar{l}-\bar{J}|P_{L=2}|\times\overline{JlJ}=\bar{l}-\bar{J}\rangle][\langle V_2\rangle_{rR}+\langle v_2\rangle_{rR}]$. v_2 was evaluated according to Eq. (16) of Ref. 4. The averages $\langle\cdots\rangle_{rR}$ were calculated with the functions $\chi_{\bar{v}\bar{J}}(r)F_{n,l}(R)$, where $F_{n,l}(R)$ denotes solution to the equation $[-(\hbar^2/2\mu)((d^2/dR^2)-(l(l+1)/R^2))+V_{0,0}(R)-e_{n,l}]F_{n,l}=0$ with $V_{0,0}(R)=V_0(R,r_0)$ and $r_0=0.766\,64$ Å.

[c]The term $\langle v_2\rangle_{rR}$ excluded from the formula for $\Delta E^{(1)}$.

TABLE V. Average levels widths, $\bar{\Gamma}_{\bar{v}\bar{J}p}$, and positions, $\bar{E}_{\bar{v}\bar{J}p}$, in Ar–HD and in Ar–$H_2$. Deviations between the values $\bar{\Gamma}$ and $\bar{E}$ listed (obtained from the XC potential) and the values resulting from the SAPT potential, $\delta_r\bar{\Gamma}$ and $\delta\bar{E}$, respectively, are shown in the second lines. Except for $\delta_r\bar{\Gamma}$ and $\bar{\Gamma}^{\text{Ar–HD}}/\bar{\Gamma}^{\text{Ar–H}_2}$, all quantities are given in cm^{-1}.

			Ar–HD			Ar–H_2			$\bar{\Gamma}^{\text{Ar–HD}}:\bar{\Gamma}^{\text{Ar–H}_2}$
$\bar{v}$	$\bar{J}$	p	$N_<$	$\bar{\Gamma}/\delta_r\bar{\Gamma}$[a]	$\bar{E}/\delta\bar{E}$[b]	$N_<$	$\bar{\Gamma}/\delta_r\bar{\Gamma}$[c]	$\bar{E}/\delta\bar{E}$[d]	
0	1	1	15	0.82	72.09				
				5	−0.02				
1	1	1	15	0.98	67.29				
				12	−0.01				
1	2	1	21	0.53	152.99	18	0.0190	323.363	28 (12)[e]
				16	0.09		−14	0.107	
		−1	13	0.22	153.96				
				24	0.23				
1	3	1	26	0.22	237.16	22	0.0042	545.014	52 (22)
				23	0.10		−19	0.115	
		−1	18	0.13	236.19	14	0.0014	546.352	93 (21)
				31	0.20		11	0.230	

[a]The averages were calculated according to the formula $\bar{X}_{\bar{v}\bar{J}p}:=(1/N)_<\Sigma^{\bar{l},J(p)}_<X_{\bar{v},\bar{J},\bar{n}=0,\bar{l},J(p)}$ for $X:=\Gamma,E$; only states of energies below the $\varepsilon_{\bar{v}\bar{J}}$ threshold were taken for the averaging; $N_<$ is the number of states summed up.

[b]The positions are relative to the $(\bar{v},\bar{J}-L)$ thresholds with $L=1$ and 2 for Ar–HD and Ar–H_2, respectively. The energies, $\varepsilon_{\bar{v},\bar{J}}$, of the thresholds $(\bar{v},\bar{J})=(0,0),(0,1),(1,0),(1,1),(1,2),(1,3)$ are: 0, 89.228, 3632.161, 3717.533, 3887.680, 4141.424 cm^{-1}—in Ar–HD, and 0, 118.487, 4161.167, 4273.742, 4497.841, 4831.392 cm^{-1}—in Ar–H_2.

[c]$\delta_r\bar{\Gamma}:=(\bar{\Gamma}^{\text{SAPT}}/\bar{\Gamma}-1)\times100\%$ and $\delta\bar{E}:=\bar{E}^{\text{SAPT}}-\bar{E}$.

[d]Empty entries mean that the states cannot decay by purely rotational predissociation.

[e]In parentheses are given the ratios of $\bar{\Gamma}$'s from which the rotational factors of the primary bound-continuum transitions involved, cf. Eq. (5), have been "removed," i.e., each $\Gamma_{\bar{v}\bar{J}\bar{n}\bar{l}J}$ taken for the averaging (a close-coupling result) was divided by $\Sigma_l|\langle\overline{JlJ}|P_L|\bar{j}-LlJ\rangle|^2$.

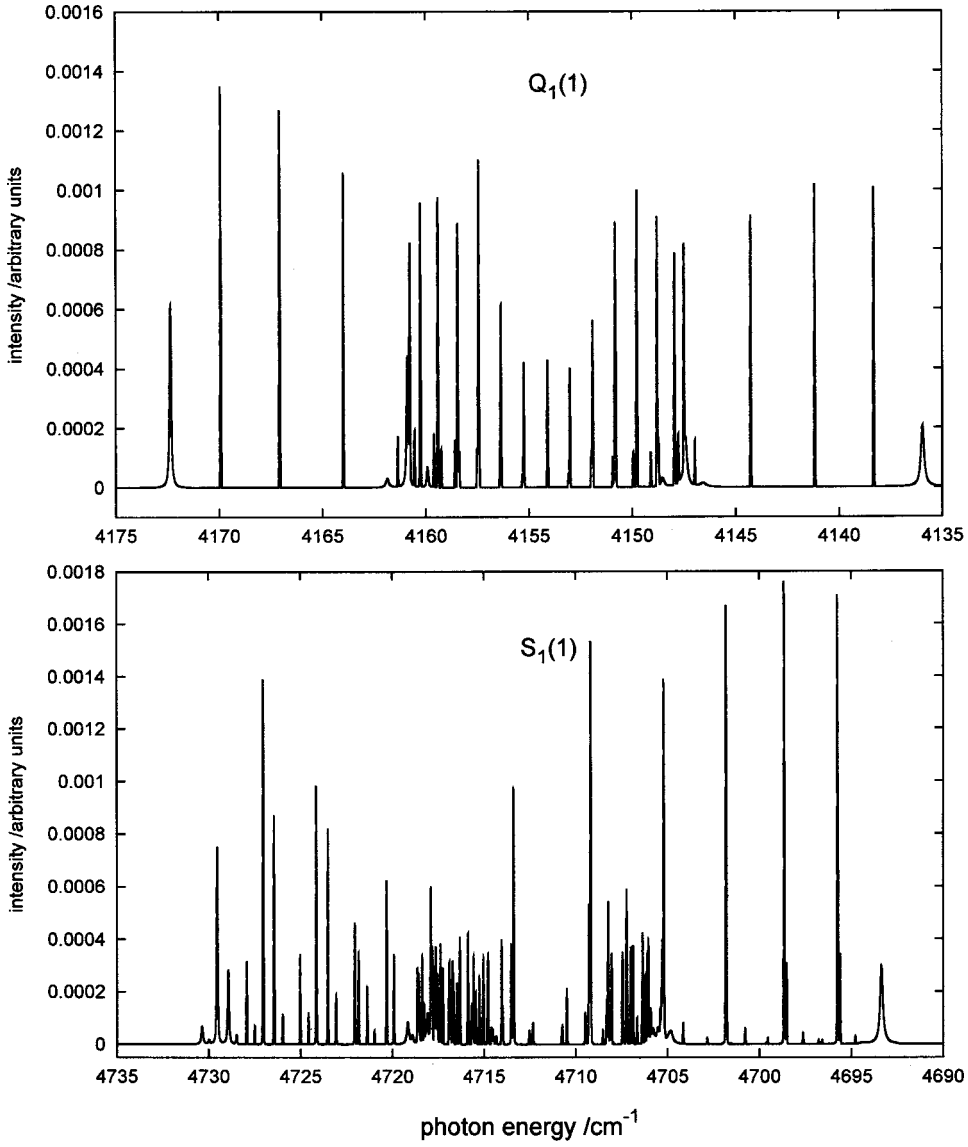

FIG. 5. Shapes of the $Q_1(1)$ and of the $S_1(1)$ bands of the absorption spectrum of Ar–H_2 determined using the XC(fit) to the intermolecular potential and the Dunker–Gordon model of the induced-dipole moment. The d_{01} strength parameter was multiplied by 3 in calculations on the $Q_1(1)$ band.

Figure 1 also shows the pronounced effects of the asymmetric isotopic substitution on stability (lifetimes) of the states: (i) the change of character of the $p=1$-parity states below the $\bar{v}=0\bar{J}=1$ thresholds, from bound states in Ar–H_2 to rapidly predissociating states (widths of the order of 1 cm^{-1}) in Ar–HD, and (ii) the quantitative change of stability of the states associated with the $\bar{v}=1\bar{J}=3$ thresholds; the widths of the states are more than 50 times larger in Ar–HD than in Ar–H_2.

An overall quantitative characterization of the rotational predissociation in the Ar–HD complex and of its enhancement in comparison with the Ar–H_2 complex is presented in Table V. Average widths $\bar{\Gamma}_{\bar{v}\bar{J}p}$ are given of the $(\bar{v},\bar{J},\bar{n}=0,\bar{l},J)$ levels with $(-1)^{j+l+J}=p$ which lie below four $(\bar{v},\bar{J}>0)$ thresholds, (0,1) and (1,1–3). The width $\bar{\Gamma}_{121}=0.53\,cm^{-1}$ characterizes the most important part of the predissociation in the Ar–HD complex, on which the previous studies focused. Relative to this quantity, the average widths of e levels associated with the other thresholds are: $\bar{\Gamma}_{\bar{v}11}/\bar{\Gamma}_{121}\approx 1.5,1.8$ for $\bar{v}=0,1$ and $\bar{\Gamma}_{131}/\bar{\Gamma}_{121}\approx 0.4$. The widths of the f levels are considerably smaller: $\bar{\Gamma}_{12-1}/\bar{\Gamma}_{121}\approx 0.4$ and $\bar{\Gamma}_{13-1}/\bar{\Gamma}_{121}\approx 0.25$. These relations between the average widths in the Ar–HD complex and the relations: $\bar{\Gamma}_{131}/\bar{\Gamma}_{121}\approx 0.22$ and $\bar{\Gamma}_{13-1}/\bar{\Gamma}_{121}\approx 0.07$—in Ar–$H_2$, reflect, of course, the dependence of the individual widths included in the averages on the two distinct factors seen in Eq. (5). The rotational factors, i.e., the Percival–Seaton coefficients, are responsible for the smaller widths of f levels. The vibrational factors, i.e., the overlap integrals of the bound and continuum radial functions, are the origin of the decrease of the widths $\bar{\Gamma}_{\bar{v}=1\bar{J}p}$ of levels of a given parity p with growing $\bar{J}$. (The overlaps tend to diminish rapidly when the position $\bar{E}_{\bar{v}\bar{J}p}$ of the levels relative to the threshold of the closest decay channel becomes higher.)

The last column of Table V presents ratios of the average widths $\bar{\Gamma}_{\bar{v}=1\bar{J}p}$ for $(\bar{J},p)=(2,1),(3,\pm 1)$ in Ar–HD relative to the widths in Ar–H_2. These ratios are meant to be a kind of global estimate of the predissociation enhancement which concerns the terminal states of transitions in the $S_1(0)$ and in

TABLE VI. $Q_1(1)$ band of Ar–H_2. Assignment of P- and R lines.

Line position (in cm^{-1})			Line position (in cm^{-1})		
Calc[b]	Calc-Expt[c]	Transitions[a]	Calc[b]	Calc-Expt[c]	Transitions[a]
4147.952	−0.030	$P_-(6,7)$, $P_-(6,5)$	4155.251	d	$R_+(0,1)$
4148.802	−0.025	$P_-(5,6)$, $P_-(5,4)$	4156.357	−0.013	$R_+(1,2)$
4149.778	−0.028	$P_-(4,5)$, $P_-(4,3)$	4157.438	−0.015	$R_+(2,3)$, $R_+(1,0)$, $R_+(2,1)$
4150.820	−0.026	$P_-(3,4)$, $P_-(2,1)$	4148.456	−0.020	$R_+(3,4)$, $R_+(3,2)$
4151.914	−0.024	$P_-(2,3)$	4159.414	−0.017	$R_+(4,5)$, $R_+(4,3)$
4153.020	···	$P_-(1,2)$	4160.268	−0.032	$R_+(5,6)$, $R_+(5,4)$
4154.101	···	$P_+(1,0)$, $R_-(0,1)$			

[a]Listed are only the transitions which contribute most significantly to the intensity of a given line. They are ordered according to the decreasing integrated intensities of the $\sigma_{f\leftarrow i}(\omega)$ profiles corresponding to them. For each line, the intensity of the last transition listed is no less than 1/3 of the intensity of the first one. The energies of the transitions are within the interval of 0.04 cm^{-1} around the line center; see Fig. 7.
[b]The position of the peak in the function $\sigma^{Ar-H_2}(\omega)$; cf. Eq. (7).
[c]The deviations are from the experimental positions taken from Ref. 2. The uncertainties of these positions are ca. 0.1 cm^{-1}.
[d]The $Q_1(1)$ line of H_2, 4155.254 cm^{-1}, is seen here in the measured spectrum.

the $S_1(1)$ bands. The estimates provided are: $\overline{\Gamma}^{Ar-HD}/\overline{\Gamma}^{Ar-H_2}=28$ and 52, respectively, for the $p=1$ states in the two bands and $\overline{\Gamma}^{Ar-HD}/\overline{\Gamma}^{Ar-H_2}=93$ for the $p=-1$ states in the $S_1(1)$ band. The numbers in parentheses indicate that more than 50% of the enhancement comes from the angular matrix element factors contributing to the widths. In view of the comment made in the previous section regarding the potential used, the estimates should be taken rather cautiously, of course. To make one aware of that, Table V also shows how the listed values of the average level widths and positions deviate from values obtained from the *ab initio* SAPT potential. For all groups of predissociating states investigated in the Ar–HD complex, the relative deviations of the widths, $\delta_r\overline{\Gamma}_{\overline{vJp}}:=(\overline{\Gamma}^{SAPT}_{\overline{vJp}}/\overline{\Gamma}_{\overline{vJp}}-1)\times 100\%$, are positive and range from $\delta_r\overline{\Gamma}_{011}=5\%$ to $\delta_r\overline{\Gamma}_{13-1}=31\%$. Two of the three deviations shown for the Ar–H_2 complex, $\delta_r\overline{\Gamma}_{121}$ and $\delta r\overline{\Gamma}_{131}$, are negative and have magnitudes (14% and 19%, respectively) comparable with their counterparts in Ar–HD. Thus, the estimates of the predissociation enhancement would be larger, even as much as 50%, if they were based on the SAPT potential.

Obviously, all the deviations $\delta_r\overline{\Gamma}$ given in Table V and also the deviations $\delta\overline{E}=\overline{E}^{SAPT}-\overline{E}$ can serve as indicators of the sensitivity of dynamics of the Ar–HD and Ar–H_2 complexes to differences which exist between particular terms of the SAPT and of the XC potentials for Ar–H_2 (cf. Figs. 2–4 of Ref. 17). The deviations in the widths of the states of the Ar–HD complex result mostly from the different slopes of the isotropic terms of the two potentials in the repulsive wall region, cf. the tests in Sec. III. The negative deviations between the SAPT and XC results obtained for the widths in the Ar–H_2 complex can certainly be attributed to the weaker repulsive part of the $L=2$ anisotropy term of the SAPT potential, seen in Fig. 4 of Ref. 17. An analysis of the deviations in energies (especially these in Ar–HD) would be more involved, but it is outside the scope of this paper.

B. Transition intensities

For reasons explained above, the simulated absorption spectrum of the Ar–H_2 complex will be presented herein. First of all, the adequacy of the used model of the induced-dipole moment function should be documented. Figure 5 serves this purpose. The contours of the $Q_1(1)$ and the $S_1(1)$ bands drawn in the two panels of Fig. 5 should be compared with the experimental views of these bands given in Ref. 3, in Figs. 5 and 6, respectively. The overall agreement of the simulated and the experimental band shapes is good, though certainly not fully satisfactory. The relations between intensities of lines from different branches of the $Q_1(1)$ band are quite well reproduced in the calculated spectrum. Less satisfactory is the consistency of the simulated and observed relative intensities between different branches of the $S_1(1)$ band. In particular, the calculated T lines appear somewhat too strong in comparison with the N lines. The cause of that is not easy to identify (the same component of the induced-dipole moment, d_{23}, is responsible for intensities in both branches). A possible explanation is that the overall relative N- to T-branch intensity in the experimental band shape may be slightly inaccurate; some minor errors can arise when the spectrum of the Ar–H_2 complex is separated from the strong underlaying CIA spectrum of H_2+Ar. The relative intensities of lines within a given branch, especially within the T- and N branches, are essentially correct in both simulated bands.

Major inconsistencies with experiment are noted only in the R- and P branches of the $Q_1(1)$ band. In particular, the two strongest lines observed in this region, at 4157.453 and 4150.846 cm^{-1}, respectively, appear in the calculated spectrum considerably weaker in comparison with their neighboring lines. However, as was revealed in Ref. 26 and is exhibited in Table VI, the strengths of majority of the R- and P lines in the $Q_1(1)$ band come from confluent intensities of at least two transitions. The two largest inconsistencies between the observed and calculated line strengths occur in the cases

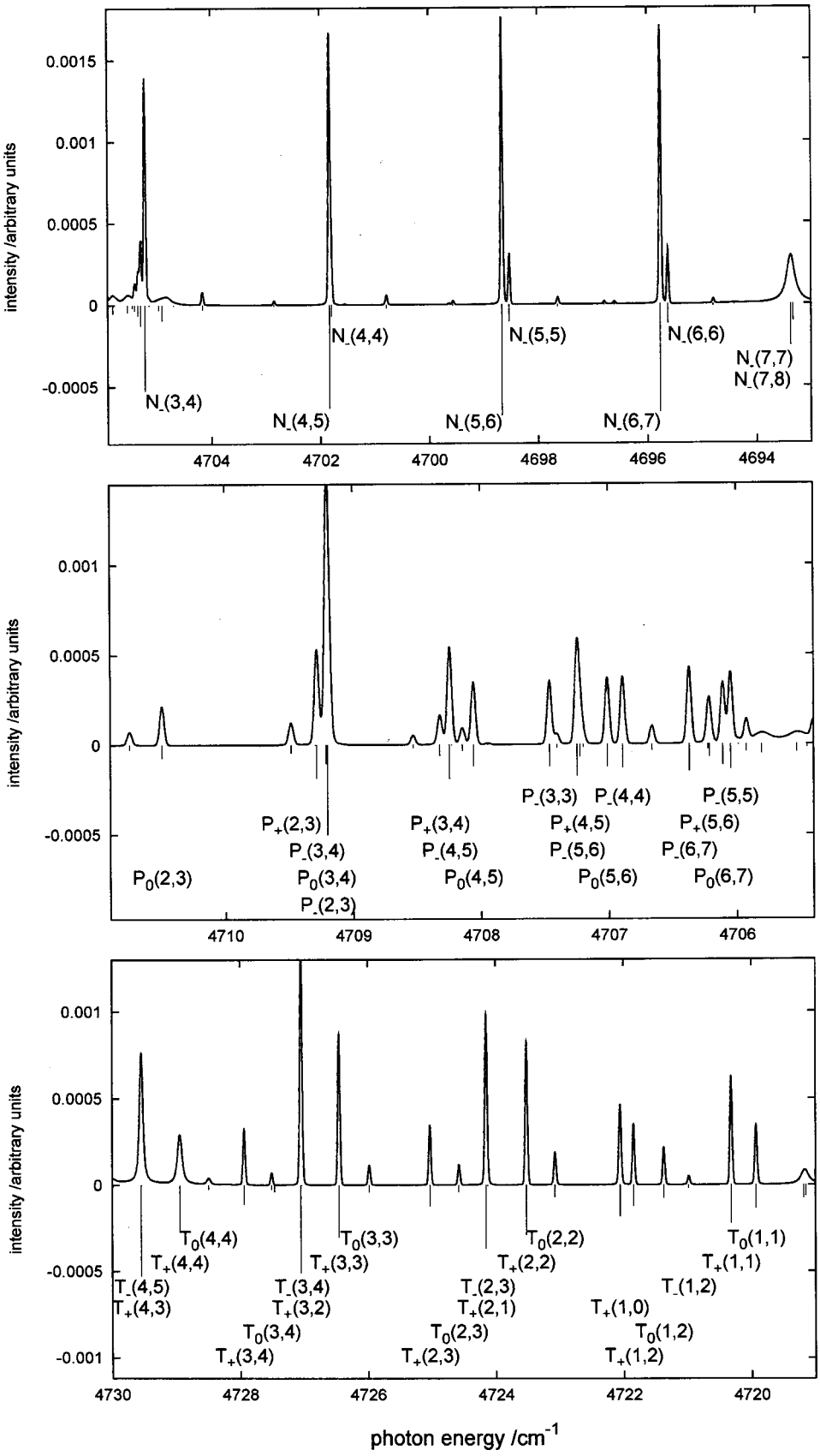

FIG. 6. Expanded views of the calculated contour of the absorption spectrum of Ar–H_2 in the N-, P-, and T branches of the $S_1(1)$ band. The contributing transitions are marked with lines in the bottom of the contour. The lengths of these lines indicate relative total intensities of the transitions.

when the contributing transitions, labeled with different $\overline{l}$'s, differ the least in their intensities. It is evident that the degree of coincidence of energies of the transitions becomes a very influential factor in these cases. Therefore, the noted inconsistencies between the calculated and measured relative intensities of the R- and P lines in the $Q_1(1)$ band should be attributed to some small inaccuracies of the intermolecular potential rather than to any serious inadequacy of the

TABLE VII. $S_1(1)$ band of Ar–H_2. Assignment of some intense lines.

Line position (in cm^{-1})			Line position	
Calc[b]	Calc-Expt[c]	Transitions[a]	Calc[b]	Transitions[a]
4693.373	0.008	$N_-(7,8)$, $N_-(7,7)$	4713.525	$R_-(2,2)$
4695.628	−0.007	$N_-(6,6)$	4714.050	$R_0(1,2)$
4695.764	0.000	$N_-(6,7)$	4715.886	$R_-(4,4)$, $R_+(2,3)$
4698.535	0.006	$N_-(5,5)$	4716.326	$R_0(4,4)$, $R_-(3,4)$
4698.667	0.001	$N_-(5,6)$	4717.918	$T_0(0,1)$, $R_0(6,6)$
4701.834	0.005	$N_-(4,5)$	4721.372	$T_0(1,2)$
4705.216	0.004	$N_-(3,4)$	4721.844	$T_+(1,2)$
4706.049	···	$P_-(5,5)$	4722.054	$T_+(1,0)$
4706.373	···	$P_-(6,7)$	4725.031	$T_+(2,3)$
4707.245	···	$P_-(5,6)$, $P_+(4,5)$	4727.939	$T_+(3,4)$
4708.245	···	$P_-(4,5)$		
4709.203	−0.027[d]	$P_-(2,3)$		
4713.399	−0.016[d]	$R_-(1,2)$		

[a]See Figs. 6 and 7.
[b]See footnote a in Table VI.
[c]Experimental positions from Ref. 3.
[d]Experimental positions from Ref. 2.

induced-dipole model used. Not disregarding the less supportive details discussed above, it seems reasonable to conclude that the comparison of the simulated and observed spectra of the Ar–H_2 complex does not raise any major doubts regarding the reliability of the information yielded by the modified Dunker–Gordon model of the induced-dipole moment on relative intensities of individual transitions.

Information obtained in the transition intensity calculations is sufficiently reliable to allow for a correct and complete assignment of lines in the parts of the spectrum where it is difficult (if not impossible) to make such an assignment based solely on the knowledge of transition energies. Thus, as an extra benefit of the calculations performed for testing the induced-dipole model(s), a complete assignment can be provided of a number of strong lines observed in the absorption spectrum of the Ar–H_2 complex. Table VI lists the most intense transitions which give rise to the 12 distinct P- and R lines seen in the $Q_1(1)$ band, cf. Fig. 5 of Ref. 3. The positions of these lines calculated from the XC potential should be close, within a few thousands of cm^{-1}, to positions which were presumably measured but not enclosed in the report from the recent experiment.[3] The results of the previous experiment[2] are used in Table VI for a comparison with the calculated positions. Note that the almost uniform shift of the calculated P- and R lines towards smaller energies, of the order of $0.02\,cm^{-1}$, is indeed close to the differences between the recent and the previous measurements of the positions of the inner N- and T lines in the $Q_1(1)$ band, cf. Table III in Ref. 3 and Table 2 in Ref. 2. Obviously, the assignment of the lines in the $Q_1(1)$ band given in Table VI is fully consistent with the information already provided in Table XIII of Ref. 26.

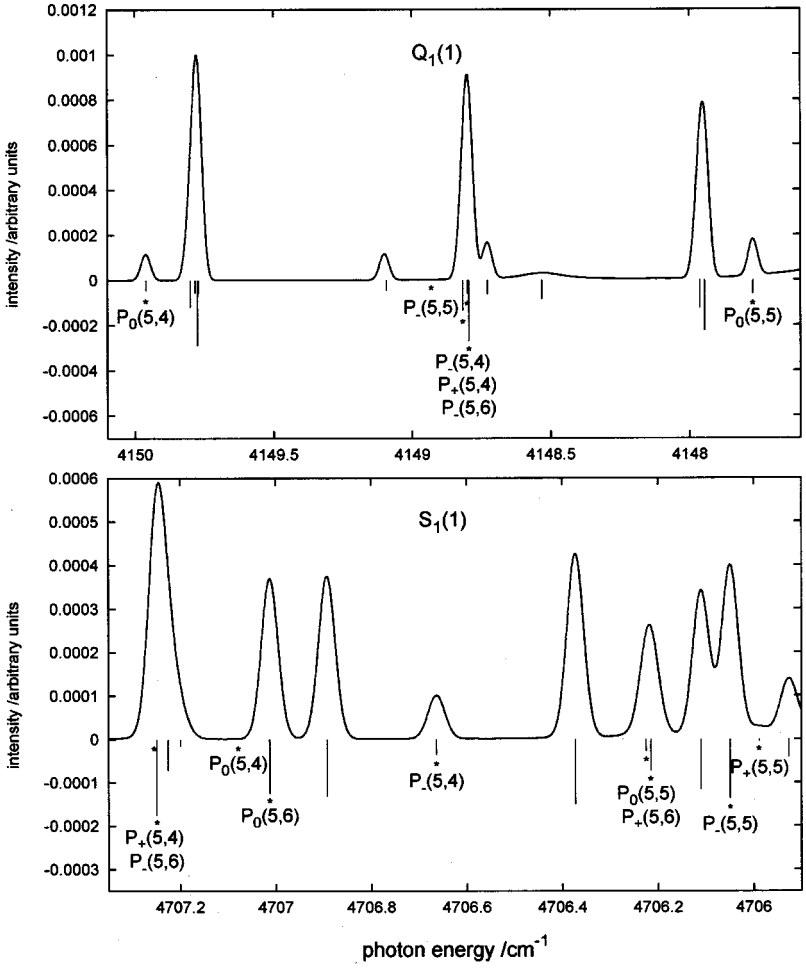

FIG. 7. Relative intensities of different components of $P(5)$ transitions in the $Q_1(1)$ and $S_1(1)$ bands of Ar–H_2 (the lines with stars in the bottom parts of the panels). The intensities and the band contour drawn in the top panel are obtained from the modified Dunker–Gordon model of the induced dipole moment [and from the model of Hutson (Ref. 28); the differences between the two models would be hardly visible in the present plot].

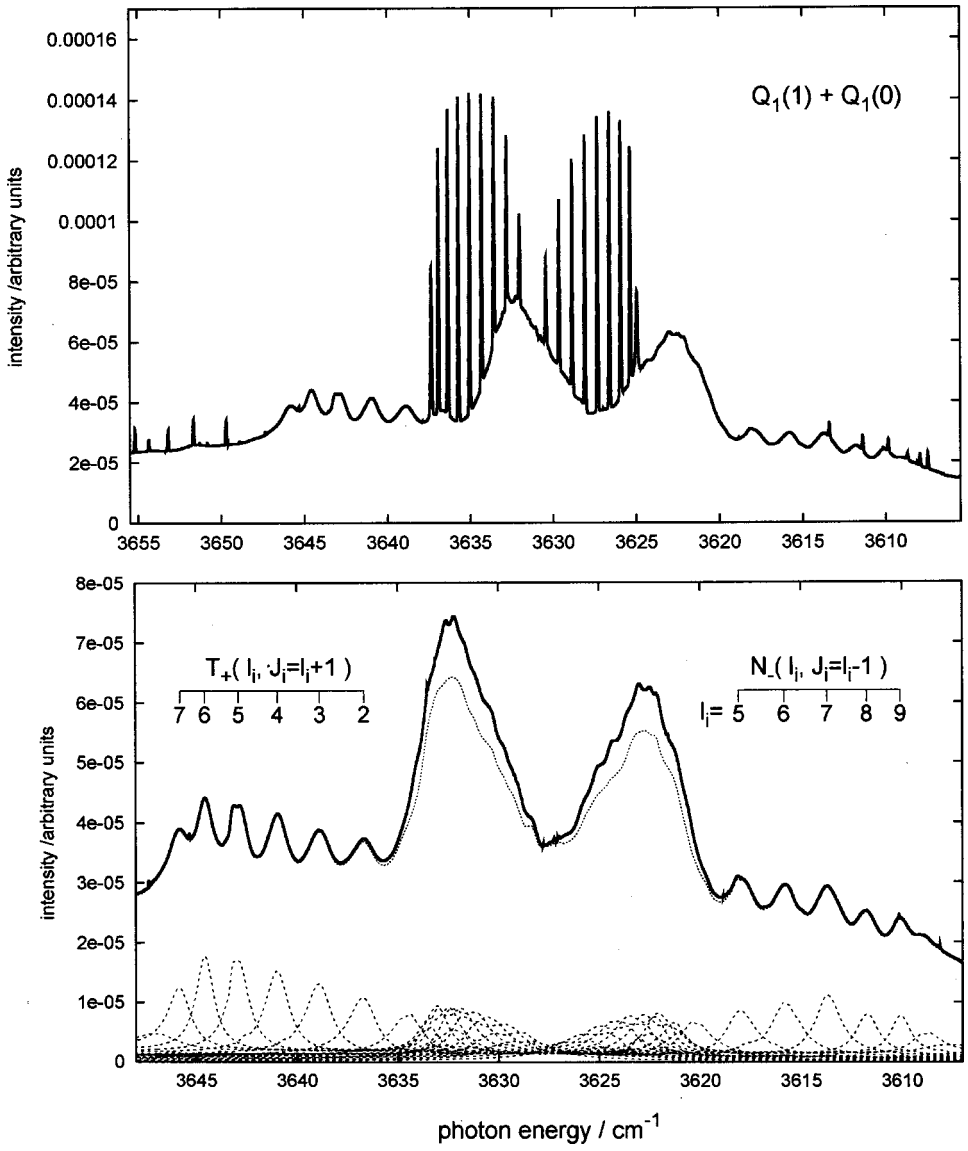

FIG. 8. Calculated shape of the absorption spectrum of Ar–HD in the photon energy region of the $Q_1(0)$ and $Q_1(1)$ bands. The small peaks at energies 3607.47, 3607.94, 3608.69, and 3609.85 cm^{-1}, are due to the $P(2)+P(1)$, $P(3)$, $R(0)$, and $R(1)$ transitions, respectively, in the $n=0 \leftarrow 1$ subband of the $Q_1(0)$ band. The two leftmost peaks seen of the $n=1 \leftarrow 0$ subband are the $R(2)$ and $P(1)$ transitions, respectively. The lower panel: The shape of the $Q_1(1)$ band. Full line—sum of all the 61 thermally averaged partial cross sections accounted for in the shape simulation, cf. Table II. Dotted line—total contribution from the 25 partial cross sections of free–free type. Dashed lines—individual $\tilde{\sigma}_{F\leftarrow F}(\omega;J_f J_i p_i)$ terms included.

Some new information emerges concerning the $S_1(1)$ band. Figure 6 presents three expanded views of the calculated contour of this band in the N-, P-, and T-branch regions, respectively. Total intensities of all the contributing transitions are shown and all but the weakest transitions are labeled. On this basis, one can complete the assignment of the lines whose positions have been measured in Ref. 3 and/or in Ref. 2. J numbers can be ascribed to the N lines and the origin of the two strong lines in the central part of the band can be identified. This information is gathered in Table VII. Moreover, it becomes possible to assign some sharp peaks clearly seen in the recorded spectrum[3] at positions not reported yet. The calculated positions of such peaks are also listed in Table VII.

Finally, let us return to the main objective of the present subsection, which is an examination of how the relative intensities of the transitions in the $Q_1(1)$ and $S_1(1)$ bands affect the shapes of these bands in the spectrum of the Ar–HD complex. Of primary importance from this standpoint are the relations between transitions which do and do not involve states of $p=-1$ parity. As pointed out in Sec. II, the $p=-1$ states are much less susceptible to the predissociation enhancement in Ar–HD, and therefore can contribute to the ''line appearance'' effect, provided that the transitions in which they participate are not too weak. The most and the least intense components of the $R(\overline{l})$- and $P(\overline{l})$ transitions in the $Q_1(1)$ and the $S_1(1)$ bands and of the $T(\overline{l})$- and $N(\overline{l})$ transitions in the $S_1(1)$ band are indicated in the diagrams drawn in Fig. 2. This crude distinction summarizes the most striking trends revealed by the intensity calculations. A detailed comparison of components of the $P(5)$ transitions in the two bands is given in Fig. 7. Note that the only transitions in the $Q_1(1)$ band which involve the $p=-1$ parity states on both ends, i.e., the $P(\overline{\overline{l,l}})$- and the $R(\overline{\overline{l,l}})$ transitions, are extremely weak. The reason for that can be easily indicated when one resorts to the formulas (4) and compares magnitudes of the angular factors $\langle 1\,\overline{l}\pm 1 J \mp 1 \| \mathcal{Y}^1_{L\Lambda} \| 1\,\overline{l} J\rangle$ of the three (L,Λ) terms, (0,1), (2,1), and (2,3), which are included in the Dunker–Gordon model of the induced dipole; it is a cancellation of the (0,1)- and (2,3) terms. Thus, no

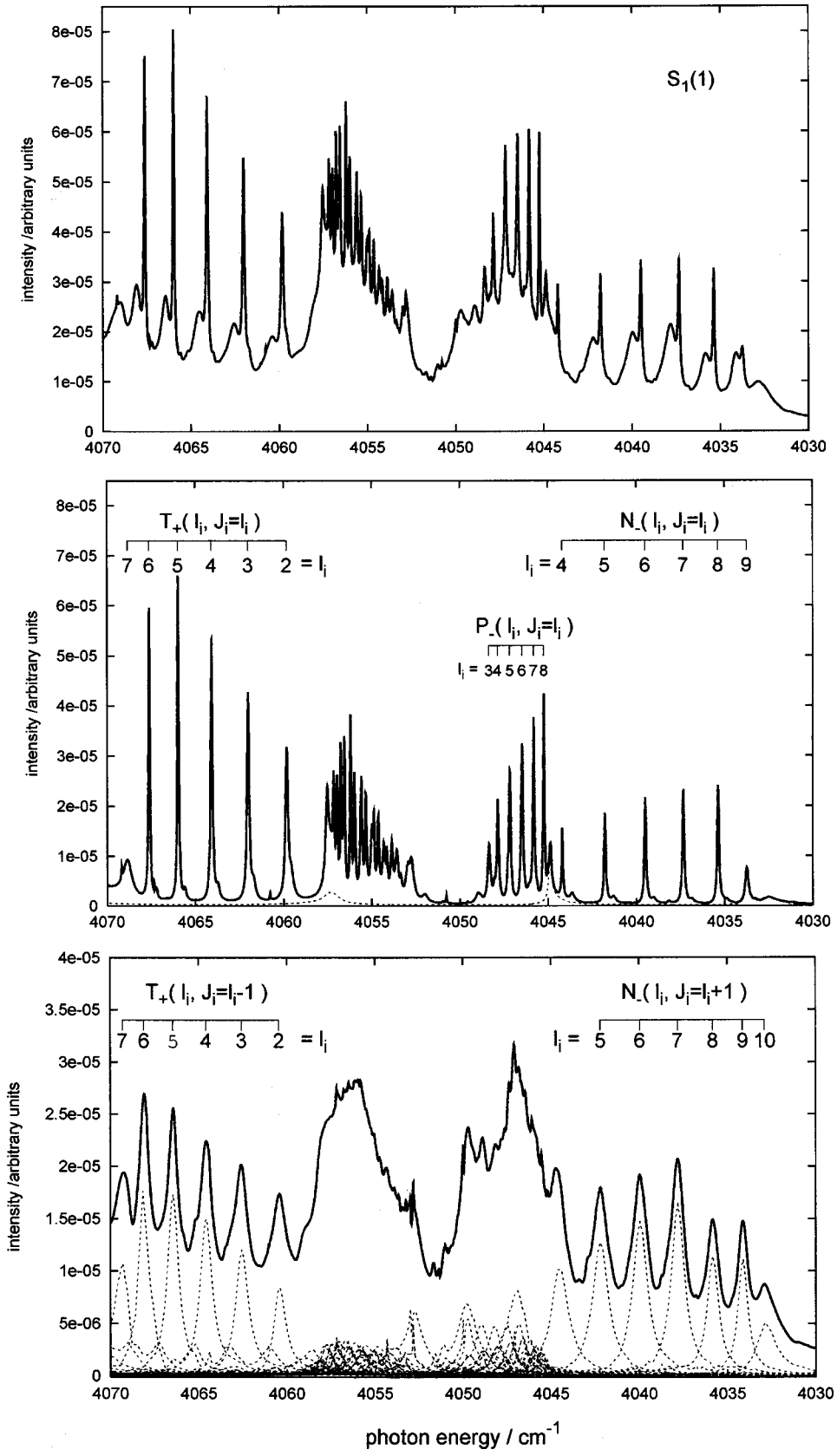

FIG. 9. Calculated shape of the $S_1(1)$ band of the absorption spectrum of Ar–HD (the top panel) and its decomposition into contributions of transitions from the initial bound and continuum $p=-1$ parity states (the middle panel) and from the initial continuum states of $p=1$ parity (the bottom panel). In the bottom part of the bottom panel are drawn the 31 individual averaged partial cross sections, $\bar{\sigma}_{F\leftarrow F}(\omega;J_fJ_ip_i)$ with $p_i=1$, specified in Table II.

sharp line is predicted to appear in the $Q_1(1)$ band of Ar–HD.

In the $S_1(1)$ band, there are six different transitions possible from a given $(\overline{l},J=\overline{l})$ level which end also on an f level. Among them, the strongest are the $T_+(\overline{l,l})$-, $P_-(\overline{l,l})$-, and $N_-(\overline{l,l})$ transitions, since their strength comes mostly from the largest $(L,\Lambda)=(2,3)$ component of the induced dipole. In the case of the medium strength

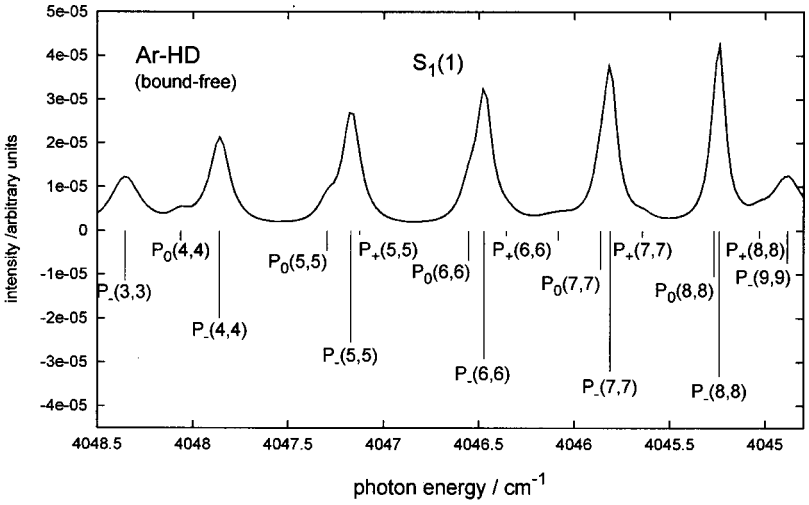

FIG. 10. Contour of the absorption spectrum of Ar–HD due to transitions from the initial $p=-1$ parity states in the region of the P branch of the $S_1(1)$ band (an expanded view of the contour from the middle panel of Fig. 9). In the bottom part: relative intensities of $P_\alpha(\overline{l},J=\overline{l})$ transitions with $\alpha=+,-,0$ (cf. Table I).

$R_\pm(\overline{l},\overline{l})$ transitions two components of the induced dipole, (2,1) and (2,3), contribute comparable amounts. The weakest $P_+(\overline{l},\overline{l})$ transitions are determined mostly by the $(L,\Lambda)=(2,1)$ component. All these transitions, except for the last one, are the strongest within their respective branches, and therefore are good candidates for causing the line appearance effect in the spectrum of Ar–HD.

C. Line shape

The calculated contours of the absorption spectrum of the Ar–HD complex in the photon energy regions of the overlapping $Q_1(1)$ and $Q_1(0)$ bands and of the $S_1(1)$ band are shown in Figs. 8 and 9, respectively. As many as 128 and 243 transitions between bound and metastable states with $\overline{n}_i=\overline{n}_f=0$ and $\overline{l}_i,\overline{l}_f=0-10$ are accounted for in the contour of the $Q_1(1)$ and the $S_1(1)$ bands, respectively. In addition, each contour carries information about several dozen weak transitions of the subbands with $\overline{n}_i=1$ and/or $\overline{n}_f=1$. The calculated lines of the $Q_1(0)$ band are drawn in Fig. 8 atop the $Q_1(1)$ contour to illustrate the emerging proportions between features of the two bands. Comparing these proportions with the measured spectrum may be a source of additional information on the adequacy of the models used for the induced-dipole moment and the intermolecular potential. Here, the point to be emphasized is that the simulated contours of the $Q_1(1)$ and $S_1(1)$ bands, compared with their counterparts for the Ar–H_2 complex (in Fig. 5) provide the ultimate confirmation of the diverse influence of the asymmetric isotopic substitution on the absorption spectrum shape. In the $Q_1(1)$ band, hardly any structure of the contour is visible in the R- and P-transition regions; certainly, no sharp peak appears to be attributed to any of the $f-f$ transitions in these regions. Only 11 broad lines due to the $T_+(\overline{l},\overline{l}+1)$- and $N_-(\overline{l},\overline{l}-1)$ transitions remain distinguishable. Almost complete intensity in the band comes, as demonstrated in the lower panel of Fig. 8, from transitions of free–free character between $p=1$ parity states. In all branches of the $S_1(1)$ band in turn, sharp lines due to the $f-f$ transitions are seen as dominant features of the contour. In the T- and N branches, these lines are superimposed on a background of broad peaks, due to the $T_+(\overline{l},\overline{l}-1)$- and $N_-(\overline{l},\overline{l}+1)$ transitions, which are counterparts of the highest lines in the spectrum of Ar–H_2 (compare Figs. 9 and 5).

It should also be pointed out that no inconsistency is encountered in the calculated contours of the Ar–HD spectrum with the predictions which were made in the previous subsection by the examination of intensities in the spectrum of Ar–H_2. This gives some evidence that the isotopic substitution transformation of the induced-dipole moment function does not introduce any qualitative changes into the spectrum shape (cf. Sec. II). Fig. 10 gives a more detailed insight into the relative intensities of transitions which result from the Dunker–Gordon model of the induced-dipole moment when it is reexpressed in the Jacobi coordinates of Ar–HD. Exhibited in this figure are the relations between the total intensities of the $\alpha=+,-,0$ components of the $P_\alpha(\overline{l},J=\overline{l})$ transitions in the $S_1(1)$ band. They look pretty much the same as the relations in the spectrum of Ar–H_2 shown in the lower panel of Fig. 7. Indeed, more precise estimations reveal that the differences do not exceed 10%. For example, the relative intensities of the transitions $P_-(5,5):P_0(5,5):P_+(5,5)$ in the $S_1(1)$ bands of Ar–HD and Ar–H_2 are 1:0.20:0.04 and 1:0.18:0.04, respectively.

Table VIII presents a quantitative characterization of the lines which are well distinguished in the calculated contour of the $S_1(1)$ band of the absorption spectrum of Ar–HD. The widths of the sharp P-, T-, and N lines are of order of $0.1-0.2\,\mathrm{cm}^{-1}$ and ca. 6–10 cm wider are the broad T- and N-lines. The sharp T- and N-lines are redshifted relative to the maxima of their closest broad lines (labeled with the same $\overline{l}$-numbers) by about $0.5\,\mathrm{cm}^{-1}$.

Obviously, the characterization of the $S_1(1)$ band provided in Table VIII and in Fig. 9 is too detailed to be verifiable by comparison with the experimental spectrum published in Ref. 1. One can merely state that the calculated positions of the pairs of the broad and sharp T- and N lines roughly agree with the maxima of the wavy contour seen in Fig. 3 of Ref. 1. The widths of the T- and N lines in the $S_1(1)$ band are presented in Fig. 11 together with the widths of lines in the corresponding regions of the $Q_1(1)$ and of the

TABLE VIII. $S_1(1)$ band of Ar–HD. Transition energies ΔE and the widths of the final (Γ_f) and initial (Γ_i) states (all in cm^{-1}). Deviations between the widths listed and the ones resulting from the SAPT potentials are shown in parentheses as $(x^{SAPT}-x)\times 100$ for $x=\Gamma_f,\Gamma_i$.

Transition[a]	ΔE	Γ_f	Γ_i[b]	Transition	ΔE	Γ_f	Γ_i[b]
$N_-(10,10)$	4032.54	0.10 (4)	1.06 (9)	$P_-(6,6)$	4046.473	0.10 (2)	
$N_-(10,11)$	4032.89	0.22 (5)	0.99 (4)	$P_-(5,5)$	4047.171	0.11 (2)	
$N_-(9,9)$	4033.76	0.11 (4)	0.11 (2)	$P_-(4,4)$	4047.859	0.12 (3)	
$N_-(9,10)$	4034.14	0.25 (8)	0.42 (3)	$P_-(3,3)$	4048.356	0.18 (7)	
$N_-(8,8)$	4035.377	0.12 (4)	0.00 (0)	$T_+(1,1)$	4057.547	0.22 (6)	
$N_-(8,9)$	4035.84	0.27 (6)	0.50 (4)	$T_+(2,2)$	4059.838	0.17 (5)	
$N_-(7,7)$	4037.348	0.12 (4)		$T_+(2,1)$	4060.45	0.29 (6)	0.52 (−9)
$N_-(7,8)$	4037.82	0.28 (7)	0.60 (5)	$T_+(3,3)$	4062.025	0.14 (4)	
$N_-(6,6)$	4039.505	0.12 (4)		$T_+(3,2)$	4062.57	0.25 (5)	0.60 (−3)
$N_-(6,7)$	4039.96	0.29 (8)	0.70 (0)	$T_+(4,4)$	4064.090	0.11 (4)	
$N_-(5,5)$	4041.793	0.11 (4)		$T_+(4,3)$	4064.59	0.21 (4)	0.60 (−1)
$N_-(5,6)$	4042.21	0.29 (8)	0.78 (7)	$T_+(5,5)$	4065.99	0.09 (3)	
$N_-(4,4)$	4044.207	0.09 (4)		$T_+(5,4)$	4066.47	0.17 (4)	0.57 (1)
$N_-(4,5)$	4044.53	0.29 (8)	0.85 (9)	$T_+(6,6)$	4067.629	0.09 (3)	
$P_-(9,9)$	4044.89	0.08 (2)	0.11 (2)	$T_+(6,5)$	4068.10	0.14 (3)	0.52 (1)
$P_-(8,8)$	4045.241	0.07 (2)	0.00 (0)	$T_+(7,7)$	4068.84	0.59 (4)	
$P_-(7,7)$	4045.813	0.09 (2)		$T_+(7,6)$	4069.31	0.53 (3)	0.46 (0)

[a]Cf. Table I.
[b]An empty entry means a bound state.

$S_1(0)$ bands. The widths calculated from the XC potential are compared with the results from the SAPT potential. Superior accuracy of the SAPT results is exhibited by enclosing the experimental data available for the $S_1(0)$ band. Using the SAPT widths as accuracy indicators, one can offer an estimation of reliability of the calculated shape of the $S_1(1)$ band. It says that all the lines may be actually wider: the sharp ones by ca. 30% and the broad T- and N lines by ca. 5% and 13%, respectively. In consequence, the disparity of heights of the lines in the pairs seen in the T- and N regions may be about 20% smaller. Thus, the predicted pattern of lines in the $S_1(1)$ band should be essentially correct.

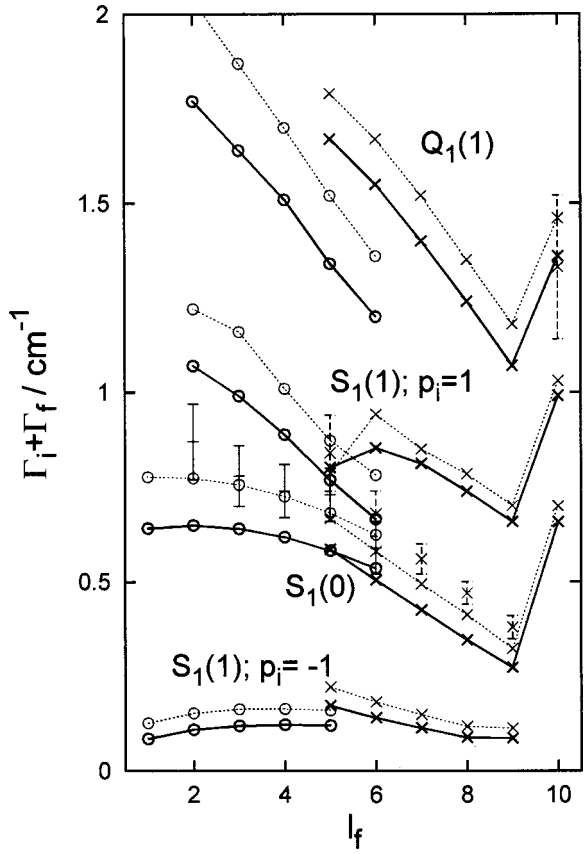

FIG. 11. Widths of T (crosses)- and N (circles) lines in the $Q_1(1)$, $S_1(0)$, and $S_1(1)$ bands of the absorption spectrum of Ar–HD. Full lines—results from XC potential, dotted lines—results from SAPT potential. For the $S_1(0)$ band, experimental data of Ref. 3 are shown with error bars.

V. CONCLUDING REMARKS

The studies of the photoabsorption dynamics presented in this paper and in Ref. 9 provide a complete theoretical description of the near-infrared absorption spectrum of the Ar–HD complex whose accuracy is the best possible at the present stage of knowledge of the intermolecular interactions (potentials). All characteristics of the spectrum (line positions, widths, relative intensities, and shapes) are determined and combined to produce the final theoretical contours of the particular bands. For the first time, included into the description are all four bands which were recorded in the first observation of Ar–HD,[1] in 1974. The bands due to the absorption by the Ar–HD($v=0,j=1$) complex were not later investigated because the experimental accuracy attainable on these bands was insufficient to extract information which could be used to generate better and better empirical potentials for Ar–H_2 (−D_2,−HD). The present work indicates that the $Q_1(1)$ and $S_1(1)$ bands of Ar–HD can serve as convenient objects for studying the interplay between bound and free components of the dynamics of photoabsorption by atom–diatom gas mixtures. These bands seem to be the first cases analyzed in which resonances in free–free phototransitions (transitions between predissociating states) manifest themselves in such a significant way. Resonances of this kind are dominant in the contour of the $Q_1(1)$ band. In the $S_1(1)$ band, they are no less important than the resonances in bound–free phototransitions. The contour of the $S_1(1)$ band

is also interesting as a carrier of the effects of the asymmetric isotopic substitution. In particular, a significant line appearance effect is encountered (consisting of an exposition of the transitions between f parity states, overwhelmed in the spectrum of Ar–H_2 by lines due to $e-e$ transitions). Obviously, it would be valuable if the pattern of lines found in the $S_1(1)$ band of the simulated absorption spectrum of the Ar–HD complex could to some extent be confirmed experimentally.

As to the methodological aspect of this work, the message is that accurate evaluation of cross sections for collision-induced absorption in atom–diatom gas mixtures, fully accounting for the anisotropy of interactions (especially as weak as that in the noble gas atom+hydrogen molecule systems), should not pose any problem when the standard invariant imbedding technique of molecular scattering, the generalized log-derivative method, is employed. However, in calculations aimed at determination of the ''proper'' CIA contours (due to direct free–free transitions), it would certainly be desirable to have at one's disposal a perturbative procedure which would make possible a substantial reduction of the effort necessary to add the structures due to transitions involving metastable states of the complex. Work on such a procedure, which will give parameters of the Fano resonance profiles in the CIA cross sections and will thereby facilitate integration over energy of initial free states, is underway.

[1] A. R. W. McKellar, J. Chem. Phys. **61**, 4636 (1974).
[2] A. R. W. McKellar, Faraday Discuss. Chem. Soc. **73**, 89 (1982).
[3] A. R. W. McKellar, J. Chem. Phys. **105**, 2628 (1996).
[4] H. Kreek and R. J. Le Roy, J. Chem. Phys. **63**, 338 (1975).
[5] J. M. Hutson and R. J. Le Roy, J. Chem. Phys. **78**, 4040 (1983).
[6] K. K. Datta and S.-I. Chu, Chem. Phys. Lett. **95**, 38 (1983).
[7] I. F. Kidd and G. G. Balint-Kurti, Chem. Phys. Lett. **105**, 91 (1984).
[8] I. F. Kidd and G. G. Balint-Kurti, Faraday Discuss. Chem. Soc. **82**, 241 (1986).
[9] F. Mrugała and R. Moszynski, J. Chem. Phys. **109**, 10823 (1998).
[10] R. J. Le Roy, G. C. Corey, and J. M. Hutson, Faraday Discuss. Chem. Soc. **73**, 339 (1982).
[11] T. Slee and R. J. Le Roy, J. Chem. Phys. **99**, 360 (1993).
[12] M. Shapiro, J. Chem. Phys. **56**, 2582 (1972).
[13] G. G. Balint-Kurti and M. Shapiro, Chem. Phys. **61**, 137 (1981).
[14] G. G. Balint-Kurti and M. Shapiro, Adv. Chem. Phys. **60**, 403 (1985).
[15] B. Jeziorski, R. Moszynski, and K. Szalewicz, Chem. Rev. **94**, 1887 (1994).
[16] H. L. Williams, K. Szalewicz, B. Jeziorski, R. Moszynski, and S. Rybak, J. Chem. Phys. **98**, 1279 (1993).
[17] C. Bissonnette, C. E. Chuaqui, K. G. Crowell, R. J. Le Roy, R. J. Wheatley, and W. J. Meath, J. Chem. Phys. **105**, 2639 (1996).
[18] G. Birnbaum, S-I Chu, A. Dalgarno, L. Frommhold, and E. L. Wright, Phys. Rev. A **29**, 595 (1984).
[19] J. Schaefer and A. R. W. McKellar, Z. Phys. D: At., Mol. Clusters **15**, 51 (1990).
[20] L. Frommhold, *Collision-Induced Absorption in Gases* (Cambridge University Press, Cambridge, 1993).
[21] F. Mrugała, Int. Rev. Phys. Chem. **12**, 1 (1993).
[22] B. R. Johnson, J. Comput. Phys. **13**, 445 (1973).
[23] F. Mrugała, J. Comput. Phys. **58**, 113 (1985); J. Chem. Phys. **93**, 1257 (1990).
[24] M. Gustafsson, L. Frommhold, and W. Meyer, J. Chem. Phys. **113**, 3641 (2000).
[25] P. S. Julienne, Phys. Rev. A **26**, 3299 (1982).
[26] A. M. Dunker and R. G. Gordon, J. Chem. Phys. **68**, 700 (1978).
[27] J. M. Hutson, Adv. Mol. Vib. Collision Dyn. **1A**, 1 (1991).
[28] J. M. Hutson, Faraday Discuss. Chem. Soc. **82**, 292 (1986).
[29] This thermally averaged photodissociation cross section is directly related to the binary absorption coefficient $\alpha(\omega)$ of the CIA theory (cf. Ref. 20): $\alpha(\omega)=n_{\mathrm{HD}}n_{\mathrm{Ar}}[1-\exp(-\hbar\omega/kT)]V\sigma(\omega)$, where V is the volume of the HD+Ar gas sample, n_{HD} and n_{Ar} are the respective number densities, and k is the Boltzmann constant.
[30] A. K. Kudian, H. L. Welsh, and A. Watanabe, J. Chem. Phys. **43**, 3397 (1965).
[31] A. K. Kudian and H. L. Welsh, Can. J. Phys. **49**, 230 (1971).
[32] Effectively, the entire component has to be slightly weakened, by a factor of $3/\sqrt{4\pi}$. This is because all the values of the strength parameter d_{01} given in Table I of Ref. 26 should be multiplied with $\sqrt{4\pi}$ to compensate for the erroneous factor in the formula for $\langle\|\mathcal{Y}^1_{01}\|\rangle$, given in Eq. (3.11) of that paper.
[33] U. Fano, Phys. Rev. **124**, 1866 (1961).
[34] F. H. Mies, Phys. Rev. **175**, 164 (1968).